Journal of Alloys and Compounds 865 (2021) 158715

Contents lists available at ScienceDirect

Journal of Alloys and Compounds

journal homepage: www.elsevier.com/locate/jalcom

On the constitution and thermodynamic modeling of the phase diagrams Nb-Mn and Ta-Mn☆

Xinlin Yan[a,1], Pavel Brož[b], Jan Vřeštál[b], Jiří Vlach[b], Jiří Buršík[c], Martina Mazalová[b], Jana Pavlů[b], Bedřich Smetana[d], Gerda Rogl[a], Markus Eiberger[a], Andriy Grytsiv[a], Herwig Michor[e], Herbert Müller[e], Gerald Giester[f], Peter Rogl[a,*]

[a] Institute of Materials Chemistry, University of Vienna, Waehringerstrasse 42, A-1090 Wien, Austria
[b] Department of Chemistry, Faculty of Science, Masaryk University, Kotlářská 2, 611 37 Brno, Czech Republic
[c] Institute of Physics of Materials, Czech Academy of Sciences, Žižkova 22, 6160 00 Brno, Czech Republic
[d] Faculty of Materials Science and Technology, VSB-TU Ostrava, 17. listopadu 15, 708 33 Ostrava, Czech Republic
[e] Institute of Solid State Physics, TU-Wien, Wiedner Hauptstrasse 8-10, A-1040 Wien, Austria
[f] Institute of Mineralogy and Crystallography, University of Vienna, Althanstrasse 14, A-1090 Wien, Austria

ARTICLE INFO

Article history:
Received 3 November 2020
Received in revised form 5 January 2021
Accepted 9 January 2021
Available online 22 January 2021

Keywords:
Intermetallics
Crystal structure
Phase diagrams
Thermodynamic modeling
Magnetic measurements
Thermal analysis

ABSTRACT

The constitution of the two phase diagrams Nb-Mn and Ta-Mn has been determined from light optical and transmission and scanning electron microscopy (LOM, TEM and SEM) with energy dispersive (EDX) as well as wavelength dispersive (WDX) X-ray spectroscopy, X-ray powder (XPD) and single crystal diffraction (XSCD), differential thermal analysis (DTA) and/or differential scanning calorimetry (DSC). The Laves phases $NbMn_2$ and $TaMn_2$ are the only binary compounds in these systems. High-temperature differential thermal analyses revealed congruent melting for $NbMn_2$ with $T_m(NbMn_2) = 1515 \pm 15$ °C, whereas $TaMn_2$ melts incongruently with $T_m(TaMn_2) = 1797 \pm 40$ °C close to a depleted peritectic reaction. Both Laves phases engage in eutectic reactions $\ell \leftrightarrow (Mn) + Nb(Ta)Mn_2$ ($T_{eut} = 1220 \pm 10$ °C at 4.9 at% Nb and $T_{eut} = 1234 \pm 10$ °C at 0.7 at% Ta, respectively). $NbMn_2$ also forms a eutectic with (Nb): $\ell \leftrightarrow (Nb) + NbMn_2$ at $T_{eut} = 1493 \pm 15$ °C and 53.2 at% Nb. Mn shows remarkably large maximum solid solubilities of 19.4 at% Mn in (Nb) as well as of 21.3 at% Mn in (Ta). Detailed atom site distribution has been established for the Laves phases by means of temperature dependent X-ray single crystal data (both C14 - $MgZn_2$-type). Combined data from XPD, EDX/WDX and SEM microstructure indicate that for both Laves phases extended homogeneity regions exist: $Nb_{1+x}Mn_{2-x}$ (62.5–73.0 at% Mn at 950°C: $-0.19 \le x \le 0.125$) and $Ta_{1+x}Mn_{2-x}$ (59.5–68.5 at % Mn: $-0.055 \le x \le 0.215$). Density functional theory (DFT) calculations favor Nb(Ta)/Mn antisite occupation rather than defects. The phases, "NbMn" and "TaMn", adopted earlier in the literature as binary system inherent compounds, were shown (TEM, WDX electron microprobe data and X-ray Rietveld refinements) to be oxygen stabilized phases of the Ti_4Ni_2O type (so-called eta(η)-phases) with modified Nb(Ta)/Mn site substitution to comply with the formula $Nb(Ta)_{3-x}Mn_{3+x}O_{1-y}$ (defect η-W_3Fe_3C-type). From magnetic susceptibility and magnetization measurements, both oxide stabilized eta phases η-$Nb_3Mn_3O_{1-y}$ and η-$Ta_3Mn_3O_{1-y}$ were found to order ferromagnetically below $T_c \sim 77$ K, but the Laves phases $NbMn_2$, $TaMn_2$ reveal weakly temperature dependent paramagnetism. No trace of the rhombohedral μ-phase (W_6Fe_7-type) has been encountered in our investigation of the two binary phase diagrams. Thermodynamic and transport properties (specific heat, electrical resistivity and magnetic susceptibility/magnetization) classify the Laves phases with metallic behavior whilst mechanical properties (elastic moduli from DFT and nanoindentation as well as hardness and thermal expansion) group both Laves phases among rather hard and brittle intermetallics. Based on (i) the experimentally derived constitution of the Nb-Mn and Ta-Mn systems, and

☆ The paper is dedicated to Prof. Dr. Wolfgang Jeitschko, in memoriam.

* Corresponding author.
E-mail address: peter.franz.rogl@univie.ac.at (P. Rogl).
[1] Current address: Institute of Solid State Physics, TU-Wien, Wiedner Hauptstrasse 8-10, A-1040 Wien, Austria.

https://doi.org/10.1016/j.jallcom.2021.158715
0925-8388/

(ii) on new own DFT data of the energy of formation of the Laves phases, a CALPHAD (CALculation of PHAse Diagrams) calculation of both systems was made providing a complete set of optimized thermodynamic data. Furthermore, the DFT calculations provided information on the instability of the η-Ta_3Mn_3 structure and the atom-site specific stabilization effect of oxygen.

1. Introduction

In diverse technological applications Nb, Ta and Mn are playing an important role such as for instance: (i) additions of Mn are able to increase the yield strength of Ti-Nb-Ta-Mn alloy foams for biomedical implants [1,2], (ii) niobium-manganese composite electrodes were found to be more suitable in supercapacitors than niobium electrodes [3]; (iii) Mn, Nb and boron additions maximize strength and toughness in martensitic micro-alloyed steels for heavy-duty engine connecting rods [4]; facilitate the production of seamless steel tubes [5]; Ta increases the pitting corrosion in super duplex stainless steels forming (Ta,Mn) - oxysulfide [6], and (iv) Hatano [7] studied the counteracting effects of Nb and Mn on microstructure and toughness for 590 MPa class low carbon bainitic steels. Nb(Ta)- or Mn-doping has been employed to improve the thermoelectric behavior of perovskite manganites [8,9], of $NbFe_{2-x}Mn_xAl$ Heusler alloys [10] and of higher manganese silicides (Nowotny chimney ladder structures) [11].

Although the knowledge of phase diagrams and thermodynamic properties is essential in defining processing conditions for optimal engineering properties, reliable phase diagram information on the basic binary systems Nb-Mn and Ta-Mn is still scarce. For a detailed summary of the experimental findings, see the compilation of binary phase diagrams in Massalski [12]. The limited experimental data available within the partial phase diagram Nb-Mn concern the region around the Laves phase (50–80 at% Mn [13]) and the Mn-rich liquidus/solidus, which has been derived from thermal analysis in the region from 88 to 100 at% Mn [14]. Interestingly the investigation of the system Nb-Mn-B at 800 °C revealed a binary NbMn phase at 45–50 at% Mn (structure undetermined, W_6Fe_7-type assumed [15]). Such a phase was later but unknowingly accounted for as a μ-phase (Nb_6Mn_7) in the thermodynamic modeling of the Nb-Mn binary as part of the Nb-Fe-Mn system [16].

From the phase diagram of the Ta-Mn system hitherto only the region from 67 to 100 at% Mn has been experimentally derived [17] with some additional data on the hardness of the $TaMn_2$-Laves phase [13]. Being unaware of an experimental diagram, Kaufman [18] produced a first thermodynamic calculation of the entire phase diagram Ta-Mn using structure-insensitive heat of formation data derived from Miedema's model [19] and early ab initio data by Colinet [20]: besides $TaMn_2$, also a compound TaMn was shown to exist. However, the Gibbs energies of phases were not based on standard SGTE unary data [21]. Although experimental data are only available for the Mn-rich part and the type and temperature of melting of $TaMn_2$ remained unclear [17], thermodynamic modeling of the entire phase diagram was performed by C. Wang et al. [22] resulting in a Mn-rich and a Ta-rich eutectic besides congruently melting $TaMn_2$ (T_m = 1670 °C). A phase "TaMn" was not considered.

The Laves phases in both systems received more attention: from high-temperature direct synthesis calorimetry measurements Meschel et al. [23] claimed a standard enthalpy of formation for $NbMn_2$ of −31.2 ± 8.1 kJ/mol.f.u. and −43.5 ± 7.5 kJ/mol.f.u. for $TaMn_2$. This experimental value for $NbMn_2$, however, appears significantly lower than the $\Delta_{298}H_f^\circ$ = −45.05 ± 3.64 kJ/mol.f.u. extracted from drop isoperibolic calorimetry in a Ni bath [24], which proved to be consistent with a density functional theory (DFT) calculation by Yan et al. [24], who arrived at −46.5 kJ/mol.f.u. These values compare well with older ab initio data by Colinet et al. (−42 kJ/mol.f.u. for $NbMn_2$ and −24 kJ/mol.f.u. for $TaMn_2$ [20]), which were evaluated within a tight-binding scheme for the *d* band – an approximate model calculation to estimate the enthalpies of formation not dealing with structure and magnetic effects. More recent ab initio calculations of Yan et al. on $NbMn_2$ also provided an eDOS (from which a gamma value of γ = 10.5 mJ/mol.K^2 is derived), as well as a full set of elastic moduli [24] (for details see Section 4.4. Hardness and mechanical properties).

With respect to (a) the absence of reliable phase diagram data in both systems Nb-Mn and Ta-Mn as well as (b) concerning the inconsistencies on the existence of the phases "Nb_7Mn_6" and "TaMn", and (c) inconsistencies in the heat of formation and the lack of physical property data for the Laves phases, the aim of the present paper is manifold: (i) to check on the crystal structure, the formation and stability of the system inherent phases particularly on the "NbMn" (Nb_7Mn_6) and "TaMn" phases, (ii) to establish reliable phase relations for the entire phase diagrams Nb-Mn and Ta-Mn, (iii) to provide physical property data for a detailed characterization of the Laves phases, (iv) to calculate via ab initio methods the energy of formation of the Laves phases, and (v) to check on the DFT stability of the "Nb(Ta)Mn" phases (particularly on η-$Ta_3Mn_3O_{1-x}$), as well as (vi) to provide a reliable set of thermodynamic data via CALPHAD modeling of both systems.

2. Experimental details

2.1. Synthesis and characterization of physical properties

The starting materials were of a minimal purity of 99.9 mass%: Ta and Nb in the form of ingot, foil or wire from Goodfellow, UK, and electrolytically deposited Mn platelets (>99.95%, Alfa Aesar, D), which were surface cleaned in concentrated HNO_3 immediately prior to use. Sample specimens (1–2 g each) were prepared from elemental pieces by either argon arc melting on a water-cooled copper hearth or on a water-cooled Hukin crucible of a high frequency (HF) furnace in Ti-gettered argon. To ensure homogenization, all alloys were re-melted several times. A slight excess of Mn was used to allow for evaporation during fusion in order to keep the total mass loss of the sample after melting below 0.5 mass%. Each alloy was weighed carefully after melting and, if necessary, Mn was added until the nominal composition was achieved after final melting. Due to the high differences in the melting points of Nb(Ta) and Mn in combination with the high vapor pressure of Mn, some of the specimens after melting and annealing still turned out to be inhomogeneous. Therefore, alloy specimens with more than 90% Mn and a total weight of 2 g were prepared from well blended powder mixtures, which were compacted in steel dies (Φ = 10 mm, without lubricant) at a pressure of 50 kg/cm^2 (~5 MPa). Nb(Ta) powders of 99.9 mass% were purchased from Sigma-Aldrich, D; Mn powder was obtained from clean Mn-pieces freshly crushed in a WC mortar (see above).

A part of each sample (within an Al_2O_3 crucible) was sealed in a silica capsule under 280 mbar Ar and heat-treated at 950 °C for about 120 h and quenched. At maximum annealing temperature the Ar-pressure inside the silica capsule reached about 1 bar and

efficiently suppressed Mn-evaporation. For annealing at 750 °C, 700 °C and 650 °C the ampullae were kept at temperature for 1 month.

X-ray powder diffraction (XPD) data from as-cast and annealed alloys were collected employing a Guinier-Huber image plate system with monochromated Fe $K_{\alpha1}$ or Cu $K_{\alpha1}$ radiation ($8° \le 2\theta \le 100°$). Precise lattice parameters were calculated by least-squares fits to the indexed θ-values with Ge as internal standard ($a_{Ge} = 0.5657906$ nm). Rietveld refinements were made with the FULLPROF program [25]. Single crystals (SC) were mechanically isolated from a crushed alloy. Inspection on an AXS D8-GADDS texture goniometer assured high crystal quality, unit cell dimensions and Laue symmetry of the single crystal specimens prior to X-ray intensity data collection on a four-circle APEX II diffractometer equipped with a CCD area detector and an Incoatec Microfocus Source IμS (30 W, multilayer mirror, Mo-K_α; $\lambda = 0.071069$ nm; detector distance of 3 cm; full sphere; $2° \le 2\theta \le 72°$). Whereas the SC of $TaMn_2$ was studied at room temperature (RT), for $NbMn_2$ we collected X-ray data at four temperatures: 100 K, 150 K, 200 K and 300 K, cooled by a continuous stream of nitrogen gas enclosing the crystal at preset temperature. Besides the general treatment of absorption effects using the multi-scan technique (SADABS; redundancy of integrated reflections >8) [26], no individual absorption correction was necessary because of the rather regular crystal shape and small dimensions of the investigated specimens ($40 \times 45 \times 60\ \mu m^3$). The crystal structure was solved applying direct methods (Program SHELXS-97) and refined against F^2 (Program SHELXL-97-2) within the programs OSCAIL or WINGX [27]. Finally, the crystal structure was standardized with the program Structure Tidy [28].

All as-cast and annealed samples were ground on SiC papers and polished with Al_2O_3 powders (down to 0.3 μm) via standard procedures and have been examined by light optical metallography (LOM) and scanning electron microscopy (SEM). The microstructure and chemical composition of the alloys were analyzed by SEM on a Zeiss Supra 55 VP equipped with an energy dispersive X-ray (EDX) detector operated at 20 kV. The non-metal content in oxygen/nitrogen/carbon stabilized impurity phases was determined from wavelength dispersive X-ray (WDX) analyses in a Jeol JSM-6460 scanning electron microscope operated at 20 kV equipped with an Oxford Instruments microanalyser using Nb/Ta-L_α, Mn-K_α, O-K_α, C-K_α, N-K_α and Si-K_α radiation and spectrometer crystals LiF (for Mn), PET (Nb/Ta), LSM60 (O, C) and LSM80N (N) (PET = Pentaerythritol, LSM60 = W-Si superlattice, LSM80N = Ni-C superlattice). Quantitative evaluation of compositions was performed with the INCA - software [29].

Thin lamellae (lateral dimensions about $10 \times 7\ \mu m^2$) for the TEM study were prepared from the Ta45Mn55 alloy after long annealing (2 months at 1000 °C) using a focused ion beam (FIB) technique in a TESCAN LYRA 3 XMU FEG/SEM×FIB scanning electron microscope. A Philips CM12 transmission electron microscope operated at 120 kV was used namely in diffraction mode.

Electrical resistivity was measured from 4.2 K to room temperature in a conventional ^{4}He cryostat, relying on an in-house equipment (error <3%). The specific resistance was obtained via a dc four-point technique using a Lake Shore Resistance Bridge 370 AC.

For specific heat measurements, we employed a Quantum Design PPMS in the temperature range from 2 to 300 K using Apiezon-N grease to ensure a good thermal contact between sample and sample platform. Temperature and field dependent magnetization data were collected at temperatures ranging from 3 to 298 K using a 6T CRYOGENIC SQUID magnetometer. Temperature dependent ac susceptibility measurements were carried out from 4.2 to 150 K with a revised Lakeshore 7000 AC Susceptometer [30], applying an ac field with an RMS amplitude of 400 A/m and a frequency of 200 Hz.

Thermal expansion from 4.2 K to 300 K was measured in a miniature capacitance dilatometer, using the tilted plate principle [31]. Three different types of equipment served to obtain hardness data (HV): (i) a microhardness tester, AD Paar MHT-4 mounted on a Zeiss Axioplan optical microscope, employing loads of 0.1, 0.5, 1, 1.5 and 2 N, applying a rate of 0.1 N s^{-1} and a loading time of 10 s, referred to as HV static, (ii) a microindenter MHT4 with a Zeiss microscope, referred to as HV dynamic (MI), using loads of 0.1, 0.5, 1, 1.5, 2, 3, 5 N and a rate of 0.1 N s^{-1} providing in parallel to HV the Young's modulus, E, from the indentation experiments, using the Poisson's ratio ν ($\nu = 0.36$ was taken from DFT calculations for $NbMn_2$ [32]) and (iii) a nanoindenter ASMEC Unat with QCSM module (Vickers Hardness Test V1, ISO 14577 standard method), referred to as HV dynamic (NI), measuring the indentations (at least 30 imprints per load and sample) with a load of 100 mN, a load rate of 100 mN/20s, an unloading rate of 10 mN/15s and providing in addition the Young's modulus for a given ν. To evaluate the hardness data of (i), the diagonal length, 2ℓ is measured and HV is calculated according to:

$$HV = \frac{0.102 \times 2F\sin\frac{136°}{2}}{(2\ell)^2} = \frac{0.1891F}{(2\ell)^2} \quad (1)$$

with F as indentation load. To get reliable results, at least 10 different impressions per load were evaluated and the error was calculated. The error for (ii) and (iii) was about 5%.

2.2. Differential thermal analysis (DTA) and differential scanning calorimetry (DSC) measurements

DTA and DSC measurements were performed on annealed samples in a Netzsch STA 409 CD/3/403/5/G apparatus within sealed quartz and/or Al_2O_3 crucibles, respectively, under a stream of 6 N argon. Sealed quartz ampules were used to prevent evaporation of volatile Mn from the samples during the measurement (technique discussed, e.g. in [33]). The equipment was calibrated in the temperature range from room temperature to 1400 °C against pure metal standards supplied by Netzsch with the accuracy to be within ± 1 °C. The measurements were performed at heating and cooling rates of 10 K/min for which the best signals vs. their separation were found. As a negligible influence of Mn evaporation on measured data was found and consistency between DTA and DSC data was observed, the DSC technique allowing measurement up to 1400 °C was preferred. Sample specimens, for which melting was anticipated above 1400 °C, were measured in Al_2O_3 and/or ZrO_2 crucibles covered by a thin sprayed-on layer of Y_2O_3 under high purity argon (6 N) at a heating rate of 15 K/min in either a DTA Setaram SETSYS 18_{TM}, a 3D DSC Setaram MHTC Line 96, or a DTA NETZSCH STA 449 F3 Jupiter.

2.3. DFT stability calculations

The ab initio calculations were performed using the Vienna ab initio Simulation Package (VASP) [34,35] within the framework of DFT. The pseudopotentials were constructed according to the projector augmented wave method [36,37], where the Perdew, Burke and Ernzerhof approximation was used to treat the exchange-correlation term [38,39]. The valence state configuration for the construction of the pseudopotentials included the 3*d* and 4*s* states for Mn, 4*p*, 5*s*, 4*d* for Nb, 6*s*, 5*d* for Ta and 2*s*, 2*p* for O. In case of the configurations $NbMn_2$, Nb_2Mn, $TaMn_2$, and Ta_2Mn of the C14 Laves phase, the optimization calculations were made with the ferrimagnetic (FIM) arrangement of magnetic moments (here, the magnetic moments of Nb and Ta have opposite direction and smaller values than those of Mn), as this arrangement of magnetic moments is more stable in comparison with the nonmagnetic (NM) arrangement [40]. The cut-off energy restricting the number of plane waves in the basis set was 550 eV for $TaMn_2$, Ta_2Mn, Ta_3Mn_3, $Ta_{48}Mn_{48}O_8$, $Ta_{48}Mn_{48}O$ and the corresponding pure elements, i.e. body-centered

tetragonal Mn (bct, being equivalent to face-centered tetragonal), body-centered cubic (bcc) Ta and the dimolecule of oxygen. For $NbMn_2$ and Nb_2Mn, bcc Nb and bct Mn (used for the evaluation of energies of formation in the Nb-Mn system), a cut-off value was set at 650 eV. Here, the bct structure corresponds to the bcc one with the *c* lattice parameter shorter than *a* and *b*. The convergence tests of total energies with respect to the number of k-points showed that the 21 × 21 × 21 k-point grid in the irreducible part of the Brillouin zone is optimal for $TaMn_2$ and Ta_2Mn, whilst a grid 13 × 13 × 7 is appropriate for $NbMn_2$ and 23 × 23 × 13 for Nb_2Mn. For Ta_3Mn_3, $Ta_{48}Mn_{48}O_8$ and $Ta_{48}Mn_{48}O$, the k-point grid was 6 × 6 × 6. For pure elements, the grid of k-points 31 × 31 × 31 was used for bcc Ta and 19 × 19 × 19 for bct Mn, both in the Ta-Mn system, and the grid 35 × 35 × 37 and 29 × 29 × 29 were used for bct Mn and bcc Nb in the Nb-Mn system. For oxygen, the k-point grid was 8 × 8 × 8. This resulted in well-converged total energies and equilibrium structural parameters, i.e. lattice parameters and internal atomic positions.

The energies of formation were calculated as the difference between the DFT total energy of the corresponding compounds and the weighted ratio of total energies of pure elements in their standard element reference (SER) states, i.e. αMn, bcc Nb, bcc Ta and O_2. In order to avoid the ab initio calculation of the complex magnetic structure of αMn, we used the total energy of the bct Mn structure with an antiferromagnetic arrangement (antiparallel orientation of magnetic moments) plus the total energy difference between α and bct Mn (1.82 kJ/mol), as calculated by Chen et al. [41], to evaluate the total energy of the SER state of αMn.

2.4. CALPHAD modeling

For thermodynamic and phase diagram calculations as well as for optimization of thermodynamic parameters based on the CALPHAD method, the Pandat software package [42] was used. Thermodynamic modeling of phases existing in the binary systems Nb-Mn and Ta-Mn relies on the well-known Compound Energy Formalism (CEF) enabling us to respect the real crystallographic structure of a phase by means of a sublattice description [43]. For the thermodynamic description of elements i in the phase ϕ, the commonly used polynomial form was applied:

$$^{0}G_i^{\phi}(T) = G_i^{\phi}(T) - {}^{0}H_i^{SER}(298.15\ K) = A + BT + CT\ln T + \sum_{n=2}^{\eta} D_n T^n, \quad (2)$$

where A, B, C, D_n and n (typically equal to 2, 3, and −1) are constants characteristic for the particular structure of the element i in a given temperature interval in Kelvin [21]. The Gibbs energy of a given ternary phase ϕ is here expressed as a sum of several contributions:

$$G_m^{\phi} - \sum_{i=Mn,Nb,Ta} x_i {}^{0}H_i^{SER}(298.15\ K) = {}^{ref}G_m^{\phi} + G_m^{\phi} + {}^{id}G_m^{\phi} + {}^{ex}G_m^{\phi}, \quad (3)$$

where ${}^{ref}G_m^{\phi}$ is the reference level of the molar Gibbs energy of a given phase ϕ, G_m^{ϕ} means Gibbs energy of formation, ${}^{id}G_m^{\phi}$ describes the molar Gibbs energy of ideal mixing of components (non-stoichiometric case) and ${}^{ex}G_m^{\phi}$ is the molar excess Gibbs energy describing a non-ideal behavior of components due to their mutual interactions [44].

The Gibbs energy of formation of the phase ϕ is expressed by the equation

$$G_m^{\phi} = \Delta H - T\Delta S, \quad (4)$$

which is used for the description of the Gibbs energies of compounds. The value of ΔH was based on DFT values of energy of formation of the phase and optimized on phase equilibrium data, similarly as ΔS. The lattice stabilities of metastable or unstable phases are calculated from first-principles now; this idea was presented first in 2001 in papers [45,46]. For the description of solubilities of components in phases, the substitutional model of the Compound Energy Formalism (CEF) Eq. (3) is used. The formula for ideal mixing:

$$^{id}G_m^{\phi} = RT\sum_{k=i,j} x_k \ln(x_k) \quad (5)$$

and the Redlich-Kister polynomial for excess contribution from interaction of components to the Gibbs energy:

$$^{ex}G_m^{\phi} = RT\sum_{n} L_n(x_i - x_j)^n \quad (6)$$

are used. In Eqs. (5) and (6) x_i, x_j, are the molar fractions of components and n is the summation index for parameters L, which may be temperature dependent.

3. Results and discussion

3.1. Crystal structure of the Laves phases $NbMn_2$ and $TaMn_2$

Both Laves phases $NbMn_2$ and $TaMn_2$ are known to crystallize with the hexagonal $MgZn_2$-type structure (C14-type). A summary of all XPD data available in the literature can be found in the compilation by P. Villars and K. Cenzual [47], however, recent single crystal X-ray work on $NbMn_2$ and $Nb_{0.87}Mn_{2.13}$ (Nb29Mn71 at%) by D. Grüner [48] was not included (details will be discussed below). So far, no detailed single crystal structure determination has been published for $TaMn_2$.

For the present work, small single crystals were broken from arc melted alloys with the stoichiometric nominal composition {Nb,Ta}Mn_2. The X-ray intensity patterns in both cases were fully indexed and were unambiguously consistent with hexagonal symmetry with space group $P6_3/mmc$ and lattice parameters: *a* = 0.48898(1) nm, *c* = 0.79970(1) nm for the Nb-crystal and slightly smaller values *a* = 0.48708(1) nm and *c* = 0.79718(1) nm for the Ta-crystal. Structure solution by direct methods yielded a fully ordered atom arrangement of $MgZn_2$-type for $NbMn_2$, whereas a minor but significant random distribution of 0.96(1) Mn1 + 0.04 Ta1 in the 2*a* site was observed for $Ta(Ta_xMn_{1-x})_2$ (x = 0.01). The refinements with anisotropic atom displacement parameters (ADPs) converged to R_{F2} = 0.0110 with residual electron densities smaller than ± 0.51 $e^-/10^{-3}nm^3$ for $NbMn_2$ (at RT) and R_{F2} = 0.0244 with residual electron densities < ± 2.40 $e^-/10^{-3}nm^3$ for $Ta(Ta_xMn_{1-x})_2$; x = 0.01, respectively. Crystallographic data for both single crystals are summarized in Tables 1 and 2. Interatomic distances are shown in Fig. 1 for $Ta(Ta_xMn_{1-x})_2$ with $0.2970 \le d_{Ta\text{-}Ta} \le 0.2990$ nm, $0.2848 \le d_{Ta\text{-}Mn} \le 0.2858$ nm, $0.2360 \le d_{Mn\text{-}Mn} \le 0.2510$ nm and are rather consistent with the sum of CN12 metal atom radii (R_{Nb} = 0.1468 nm, R_{Ta} = 0.1467 nm and R_{Mn} = 0.1304 nm [49]). Whereas distances Ta-Ta are slightly longer than the sum of radii, distances Mn-Mn for site 6*h* are shorter by about 10% and for Mn-Mn (2*a* to 6*h*) are shorter by about 5% indicating a strong Mn-Mn interaction. Such a behavior is also inherent to $NbMn_2$. Our room temperature atom parameters for $NbMn_2$ are essentially consistent with the findings of Grüner [48], although his atom parameters are slightly higher and his lattice parameters are somewhat lower.

Evaluation of the temperature dependent X-ray single crystal intensity data sets in Table 2 clearly document that $NbMn_2$ adopts the $MgZn_2$-Laves type at all the four temperatures measured, namely: 100 K, 150 K, 200 K and 300 K. In combination with XPD data up to the melting point we observe that no phase transition appears within the entire temperature interval (100–1788 K). $TaMn_2$ displays analogous behavior (298–2070 K).

The temperature dependence of the lattice parameters of $NbMn_2$ for the temperature range from 100 to 300 K, as depicted in Fig. 2 (top), shows a rather smooth variation within ~2 permille. Fig. 2

Table 1
Structural data for $Ta(Ta_xMn_{1-x})_2$ (x = 0.01) from X-ray single crystal measurement at 300 K. Partially ordered $MgZn_2$-type; space group $P6_3/mmc$; No. 194; structure standardized with program *Structure Tidy* [28]. Anisotropic atomic displacement parameters U_{ij} in [10^2 nm^2].

Parameter/compound	Crystal data
Phase composition (EDX, at%)	Ta35Mn65 ≡$Ta_{1.05}Mn_{1.95}$
Refinement composition (at%)	$Ta_{1.02}Mn_{1.98}$ ≡$Ta(Ta_xMn_{1-x})_2$; x = 0.01
Structure type	$MgZn_2$-type
θ range (deg)	5.1 ≤ 2θ ≤ 72.5
Crystal size	65 × 70 × 80 μm^3
$a = b$ (nm)	0.487077(7)
c (nm)	0.797175(11)
Reflections in refinement	182 ≥ 4σ(F_o) of 182
Number of variables	12
Mosaicity	<0.49
$R_{F2} = \Sigma\lvert F_o^2-F_c^2\rvert/\Sigma F_o^2$	0.0244
wR2	0.0582
R_{Int}	0.069
GOF	1.278
Extinction (Zachariasen)	0.0011(8)
M1 in 2*a* (0,0,0); occ.	**0.96(1) Mn1 + 0.04 Ta1**
$U_{11} = U_{22}$; U_{33}; U_{12}; $U_{23} = U_{13} = 0$	0.0029(8); 0.0028(9); 0.0015(4)
Ta2 in 4*f* (⅓, ⅔, *z*); occ.	*z* = 0.56376(6); 1.00(1)
$U_{11} = U_{22}$; U_{33}; U_{12}; $U_{23} = U_{13} = 0$	0.0027(2); 0.0036(3); 0.0014(1)
Mn2 in 6*h* (*x*, 2*x*, ¼); occ.	*x* = 0.1718(2); 1.00(1)
U_{11}; U_{22}; U_{33}; U_{12}; $U_{23} = U_{13} = 0$	0.0009(4); 0.0005(5); 0.0025(5); 0.0003(3)
Residual electron density; max; min in (electron/nm^3) × 10^3	2.40 (0.134 nm from Mn2); −1.76
Interatomic distances < 0.3 nm (standard deviation <0.0004)	
Ta – 3 Mn2	0.2848
Ta – 6 Mn2	0.2853
Ta – 3 Mn1	0.2858
Mn1 – 6 Mn2	0.2464
Mn1 – 6 Ta	0.2858
Mn2 – 2 Mn2	0.2360
Mn2 – 2 Mn1	0.2464
Mn2 – 2 Mn2	0.2510
Mn2 – 2 Ta	0.2848
Mn2 – 4 Ta	0.2853
Ta – 1 Ta	0.2970
Ta – 3Ta	0.2990

(middle) denotes the variation with T of the atom parameters in the various Wyckoff sites for $NbMn_2$. Although the *z* parameter of the Nb-atoms in 4*f* seems to constantly rise with temperature, the *x* parameter of the Mn-atoms in the 6*h* site passes through a maximum at 150 K.

Fig. 2 (bottom) (100–300 K) portraits the temperature dependence of the interatomic distances in $NbMn_2$, which merely reflects the variation of lattice parameters in combination with the atom parameter variation vs. T. Consequently, all distances between Mn atoms rise rather monotonically with temperature within 2 permille. For the evaluation of the Debye temperature from the temperature dependent ADPs see Section 4.2. Specific heat.

In this context, it is interesting to note that D. Grüner [47] observed a weak 2*a*×2*a*×2*c* superstructure of the $MgZn_2$-type on polycrystalline residues, which were extracted by diluted HCl from arc melted Mn-rich alloys Nb10Mn90 (in at%), sealed in Nb-vessels and annealed at 1100 °C. No structural details were reported, but it was said that single crystals $Nb_{0.87}Mn_{2.13}$ (Nb29Mn71 at%), extracted in the same way from Mn-rich alloys, did not show any superstructure reflections and clearly revealed isotypism with the $MgZn_2$-type. The random distribution of (3.48Nb+0.52Mn) in the 4*f*-sites in the Mn-rich single crystal $Nb_{0.87}Mn_{2.13}$ [48] is in line with random distributions of (0.1Nb+1.9Mn) in the 2*a* sites and (0.22Nb+5.78Mn) in the 6*h* sites for the Nb-rich alloy $Nb_{1.08}Mn_{1.92}$ (Rietveld refinement data in Table 2). It should be mentioned here, that our XPD neither in Nb-Mn nor the Ta-Mn system detected any superstructure reflections.

3.2. The oxygen-stabilized phases "NbMn" (≡ $Nb_3Mn_3O_{1-y}$) and "TaMn" (≡ $Ta_{3-x}Mn_{3+x}O_{1-y}$)

Our recent attempts to get a phase-pure compound $NbMn_2$ [24], revealed that in Nb-rich samples small amounts of a second compound richer in Nb caused the appearance of weak ferromagnetism. EDX measurements yielded a phase composition close to NbMn. Further experiments gave clear hints that the percentage of this phase in Nb-Mn and also in Ta-Mn alloys increases with the non-metal impurity content (from WDX predominantly oxygen, no nitrogen, no carbon) in the raw elements (such as Mn or Nb/Ta-powder). Therefore, the new secondary phase was concluded to be an impurity stabilized ternary phase. Indeed, painstaking attempts to reduce the oxygen-level of the starting ingot materials as well as in the preparation (melting under high purity argon, handling materials exclusively in a <3 ppm (O+H_2O) glove box system) were finally successful yielding phase pure and paramagnetic Laves phases $NbMn_2$ [24] and $TaMn_2$ (this work). Laves phase samples without any traceable amounts of the magnetic phase have been obtained with an addition of 1–2 mass% of lanthanum metal as an internal oxygen getter obviously capturing the oxygen and forming a „nonmagnetic" $LaMn_xO_y$ phase, which did not disturb the magnetic characterization of the Laves phases (see below Section 4.1 Susceptibility).

In this paper we adopted a "dirty way" to increase the amount of this impurity stabilized phase by melting powder compacts in the region Nb to NbMn (and Ta to TaMn) in an argon arc-melter with intermittent crushing the buttons in air and adding Mn to compensate fusion losses. Various oxygen contents were introduced by adding proper amounts of MnO_2 or Nb_2O_5 and Ta_2O_5. In a few cases, we also tried to start from fine powder compacts that were reacted in a sealed quartz tube for 3 × 36 h at 950 °C with intermittent crushing in air and re-compacting. Although the new phase formed in larger quantities, we were unable to synthesize a single-phase sample in both systems. The spectra usually contained the Laves phase as the dominant phase and the "impurity phase" in addition.

At this stage, a series of selected area electron diffraction (SAED) patterns in Fig. 3 were obtained via TEM from thin lamellae prepared in SEM by FIB from the white phase in the cast alloy Ta50Mn50, which was annealed for 2 months at 1000 °C. Their analyses prompted a face-centered cubic (fcc) lattice with a lattice parameter $a \sim 1.12$ nm (averaged from a set of axes, [100], [110], [111], [210], [310] and [510]). On the basis of this information, the indexation of the X-ray powder intensity pattern of the new phases in both systems was successful. A search for the structure type in crystal databases such as in Pearson's Crystal Data [47] and in ICSD [50], employing fcc crystal symmetry with a range of lattice parameters $a = 1.13 \pm 0.1$ nm prompted directly the CdNi-type (of HfMn), which in fact is an occupation variant of the Ti_2Ni-type (eta(η)-phase).

The mode of atom site occupation and filling the octahedral voids in the various composition variants of the so-called η-phases deriving from the parent Ti_2Ni-type was already extensively discussed by Rogl et al. [51]. Referring to this analysis, the phases $Nb_{\sim 1}Mn_{\sim 1}O_y$ and $Ta_{\sim 1}Mn_{\sim 1}O_y$ have to be classified as a filled metal host lattice structure where the manganese atoms in 16*c* of space group $Fd\bar{3}m$ (origin at center of symmetry) fill the centers of metal icosahedra (each formed by six Nb(Ta)/Mn atoms from the sites 48*f* and 32*e*) yielding a formula $Nb(Ta)_{\sim 3}Mn_{\sim 3}O_y$. Generally in eta-phases, nonmetal atoms such as C, N or O are assumed to occupy the octahedral voids in 16*d*, but may also enter a second set of octahedral voids in Wyckoff site 8*b* (⅜,⅜,⅜). It may be noted here that Wyckoff site 8*b* changes to site 8*a* (⅛,⅛,⅛) in the non-standardized structure (using $Fd\bar{3}m$ with the origin at $-43m$). We used this standardized starting model for Rietveld refinements to elucidate the final atom distribution in the novel compounds $Nb_{\sim 1}Mn_{\sim 1}O_y$ and $Ta_{\sim 1}Mn_{\sim 1}O_y$. As the situation is quite similar for both systems Nb(Ta)-Mn, we may further on focus here on the alloys from the Ta-Mn system.

Table 2
Structural data for $NbMn_2$ from X-ray single crystal measurement at four different temperatures. Partially ordered $MgZn_2$-type; space group $P6_3/mmc$; No. 194; origin at center; structure standardized with program *Structure Tidy* [28]. Anisotropic atomic displacement parameters U_{ij} in [10^2 nm^2]. Interatomic distances < 0.3 nm.

Parameter/Alloy composition	$NbMn_2$			
Temperature	Room temperature	200 K	150 K	100 K
a=b (nm); *c* (nm)	0.48898(1); 0.79970(1)	0.48834(1); 0.79853(2)	0.48824(1); 0.79823(1)	0.48801(1); 0.79798(1)
Data collection, 2Θ range	2 < 2Θ < 72.73	2 < 2Θ < 72.39	2 < 2Θ < 72.41	2 < 2Θ < 72.44
Reflections in refinement	173 F_o > 4σ(F_o) of 184	172 F_o > 4σ(F_o) of 182	175 F_o > 4σ(F_o) of 181	170 F_o > 4σ(F_o) of 182
Mosaicity	< 0.43	< 0.43	< 0.43	< 0.43
Number of variables	11	11	11	11
$R_F^2 = \Sigma\|F_o^2-F_c^2\|/\Sigma F_o^2$	0.0110	0.0210	0.0158	0.0118
R_{Int}	0.0265	0.0296	0.0299	0.0269
GOF	1.901	2.072	2.178	2.183
Extinction (Zachariasen)	0.014(1)	0.015(1)	0.015(1)	0.016(1)
Nb1 in 4*f* (1/3,2/3,*z*); occ.	*z* = 0.56349(3); 1.00 Nb	*z* = 0.56347(4); 1.00 Nb	*z* = 0.56339(4); 1.00 Nb	*z* = 0.56337(4); 1.00 Nb
U_{11} = U_{22}; U_{33};	0.0051(1); 0.0051(1);	0.0038(1); 0.0036(2);	0.0031(1); 0.0030(1);	0.0027(1); 0.0025(1);
U_{12}	0.0025(1)	0.0019(1)	0.0015(1)	0.0014(1)
Mn1 in 2*a* (0,0,0); occ.	1.00 Mn	1.00 Mn	1.00 Mn	1.00 Mn
U_{11} = U_{22}; U_{33};	0.0051(2); 0.0043(3);	0.0038(2); 0.0029(3);	0.0030(2); 0.0023(3);	0.0026(2); 0.0022(3);
U_{12}	0.0026(1)	0.0019(1)	0.0015(1)	0.0013(1)
Mn2 in 6*h* (*x*,2*x*,¼); occ.	*x* = 0.17128(4); 1.00 Mn	*x* = 0.17136(5); 1.00 Mn	*x* = 0.17139(5); 1.00 Mn	*x* = 0.17133(4); 1.00 Mn
U_{11}; U_{22};	0.0048(1); 0.0045(2);	0.0036(2); 0.0035(2);	0.0030(2); 0.0030(2);	0.0026(2); 0.0026(2);
U_{33}; U_{12}	0.0051(3); 0.0023(1)	0.0034(2); 0.0017(1)	0.0029(2); 0.0015(1)	0.0025(2); 0.0013(1)
Residual electron density; max; min in (e/nm^3) x 1000	0.51; −0.50; 0.097 nm from Mn1	1.11; −1.12; 0.135 nm from Mn2	0.98; −0.79; 0.149 nm from Nb1	0.72; −0.67; 0.160 nm from Mn2
Nb1 – 3 Mn2	0.2858	0.2854	0.2852	0.2851
Nb1 – 6 Mn2	0.2864	0.2860	0.2860	0.2859
Nb1 – 3 Mn1	0.2868	0.2865	0.2864	0.2862
Mn1 – 6 Mn2	0.2470	0.2467	0.2466	0.2465
Mn1 – 6 Nb1	0.2868	0.2865	0.2864	0.2862
Mn2 – 2 Mn2	0.2377	0.2373	0.2372	0.2372
Mn2 – 2 Mn1	0.2470	0.2467	0.2466	0.2465
Mn2 – 2 Mn2	0.2513	0.2510	0.2510	0.2508
Mn2 – 2 Nb1	0.2858	0.2854	0.2852	0.2851
Mn2 – 4 Nb1	0.2864	0.2860	0.2860	0.2859
Nb1 – 2 Nb1	0.2983	0.2979	0.2979	0.2979
Nb1 – 2 Nb1	0.3000	0.2996	0.2995	0.2994

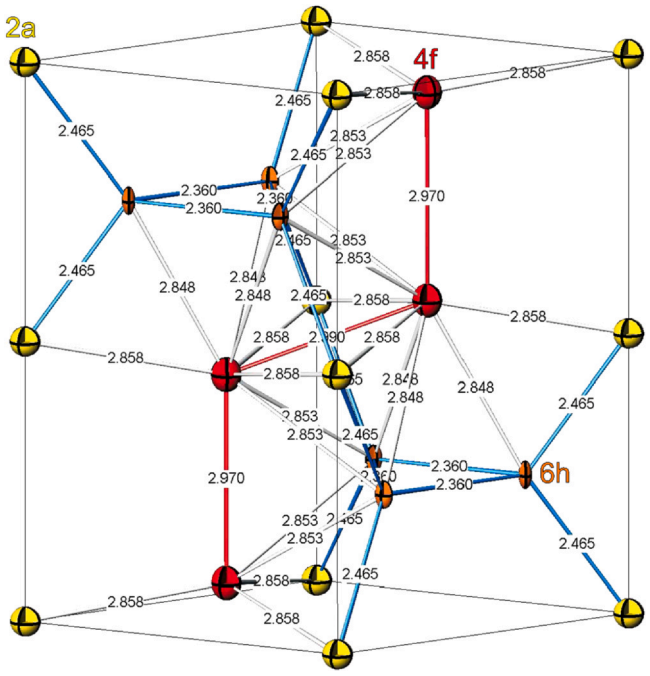

Fig. 1. Crystal structure of $TaMn_2$ ($Ta_{1.02}Mn_{1.98}$) in three-dimensional view with bond distances (in Å). Atoms are displayed with their anisotropic thermal displacement ellipsoids as derived from X-ray single crystal refinement (see Table 1). Mn1 atoms in site 2*a* are yellow (0.96 Mn1 + 0.04 Ta1); Mn2 atoms in site 6*h* are ocher; Ta2 atoms in site 4*f* are red. (For interpretation of the references to colour in this figure legend, the reader is referred to the web version of this article.)

Rietveld refinement of an arc melted alloy Ta43Mn57 (see Fig. 4) clearly showed that the composition of the new phases appears close to a ratio (Nb,Ta):Mn ~ 1:1 rather than to a ratio (Nb,Ta):Mn ~4:2 such as is typical for many oxygen-stabilized compounds deriving from the Ti_2Ni-type (Ti_4Ni_2O) (eta(η)-phase; for representatives see Pearson's Crystal Data [47]). Although the hexagonal Laves phase $Ta_{0.9}Mn_{2.1}$ ($MgZn_2$-type) with 85 vol% is the dominant phase in the X-ray powder diffraction pattern, the secondary phase of this pattern can clearly be indexed on an fcc lattice (*a* = 1.14546(1) nm), fully consistent with the structure model discussed above. The results of the refinement are listed in Table 3. These results reveal only slight deviations from a full atom order with a random atom distribution of (43.6 Ta+4.4 Mn) atoms in the 48*f* site, (1.0 Ta+31.0 Mn) atoms in the 32*e* site and exclusively Mn in the 16*c* site. Interestingly the refinement refuses any oxygen in the Wyckoff sites 8*a* and 8*b* but readily accepts 5.34 O atoms in the 16*d* site of the space group $Fd\bar{3}m$ (origin at center). From this atom distribution, we arrive at a chemical formula $Ta_{2.78}Mn_{3.22}O_{0.33}$ ($Ta_{3-x}Mn_{3+x}O_{1-y}$; x = 0.22, y = 0.67), which directly complies with the proto-type of W_3Fe_3C as one of the structure variants of the Ti_4Ni_2O family [47,51]. The small deviations from full stoichiometry ($Ta_{2.78}Mn_{3.22}O_{0.33} \equiv$ Ta43.9Mn50.9O5.2 in at%, i.e. at a ratio Ta:Mn = 46.3:53.7) are well reflected in the EDX/WDX-compositions derived by the X-ray microanalyses. The intensity simulations for the SAED-patterns, calculated for the structure model of $Ta_{2.78}Mn_{3.22}O_{0.33}$ (plotted in Fig. 3 in the JEMS software [52,53]) are fully consistent with the observed patterns. It should be mentioned here that the appearance of oxygen exclusively in Wyckoff site 16*d* rules out the structure type of W_6Fe_6C (where the nonmetal atom only enters the 8*b* site but leaves the 16*d* site empty).

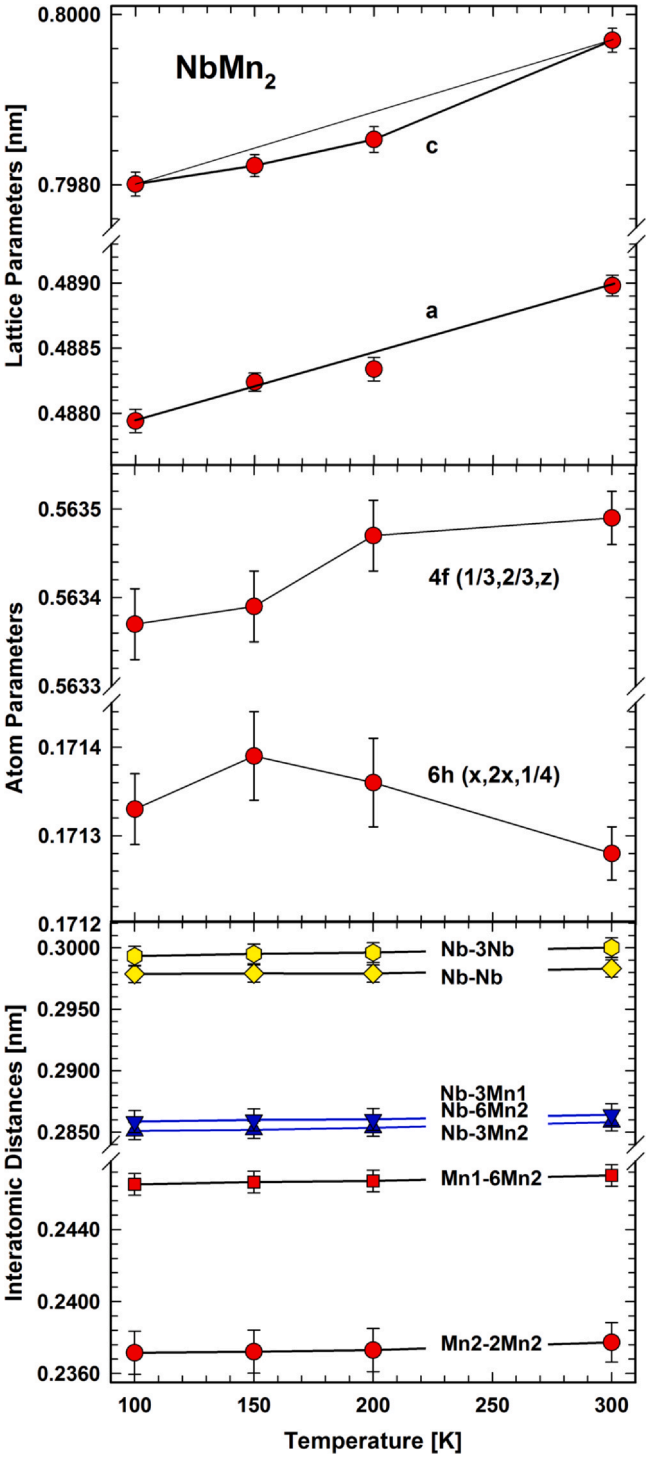

Fig. 2. Structure parameters for $NbMn_2$ in the temperature range from 100 to 300 K (from X-ray single crystal data, Table 2). Top: thermal expansion of the lattice parameters; middle: atom parameters for the various Wyckoff sites; bottom: interatomic distances. The distance $d_{Mn2-2Mn2}$ = 0.25130 nm (towards the neighboring unit cell) at 300 K with almost no variation is not shown here.

After annealing at 950 °C for 4 days the XPD pattern of the cast alloy Ta43Mn57 has changed, i.e. besides the Laves phase as the dominant phase, we now encounter two of the fcc eta-phases in the SEM analysis as well as from Rietveld refinement (see Table 3). Interestingly the Laves phase (~81 vol%) appears practically stoichiometric but with slightly lower lattice parameters. The secondary phases can both be described with the W_3Fe_3C-type but contain rather small contents of oxygen: $Ta_{2.84}Mn_{3.16}O_{0.23}$ (14 vol%, a = 1.14088(1) nm) and $Ta_{3.01}Mn_{2.99}O_{0.13}$ (4 vol%, a = 1.12859(2) nm). Random distributions of Ta/Mn atoms only appear in the 48*f* site and are of smaller extent, therefore the formulae are close to full order; the main difference is the oxygen content reflected also by the different unit cell dimensions. It is unclear if the sample reveals a transition state to final equilibrium or if the two eta-phases are equilibrium phases of the Ta-Mn-O system.

The ferromagnetic impurity phase, which appeared in small quantities during the attempts to prepare single phase $NbMn_2$ was equally well described by a W_3Fe_3C-type eta-phase (for details see the Rietveld refinement of alloy Nb40Mn60, annealed at 900 °C, in Table 3 and Fig. S1 of Supplementary Material). Rietveld and EDX analyses agree on a formula $Nb_{2.86}Mn_{3.14}O_{0.31}$ ($Nb_{3-x}Mn_{3+x}O_y$; x = 0.14, y ~ 0.69) with a lattice parameter a = 1.13415(2) nm.

Finally, a search for representatives of the W_3Fe_3C type in Pearson's Crystal Data [47] indeed revealed the eta-phase Ta_3Mn_3O, as reported by Schönberg [54]. Although Schönberg investigated the Ta-Mn-O system (<50 at% O), he was unable to obtain the eta-phase in a pure condition but rather "in the presence of fairly large amounts of other phases". However, neither the Ta-Mn-O phase equilibria nor a structure refinement of the eta-phase have been given; only the range of lattice parameters was listed from 1.115 to 1.118 nm [54], which, however, is much smaller than the unit cells derived from our samples. Interestingly, Schönberg's investigation of the Ta-Mn-N system [55] did not yield any η-phase, in contrast to findings of Holleck et al. [56], who was able to synthesize both eta-nitrides: $Nb_{3.5}Mn_{2.5}N$ (a = 1.142 nm) and Ta_3Mn_3N (a = 1.135 nm). Here it should be emphasized that our WDX test on N in our eta-phases was always negative.

The formation of eta-phases in Ta-Mn alloys can be best seen in Fig. 5 from an HF melted alloy $TaMn_2$, prepared from Ta-foil and pieces of Mn. The evaluation of the microstructure by means of SEM-EDX and WDX revealed a partially melted Ta-foil surrounded by liquid Mn, which solidified in layers of eta-phases and finally the Laves phase (for details see Fig. 5).

3.3. Constitution of the systems Nb-Mn and Ta-Mn

In order to provide a thorough constitutional basis for proper thermodynamic modeling, we have started with DTA/DSC investigations. As the hitherto known information suggested melting temperatures for the sections T - TMn_2 (T = Nb,Ta) above 1400 °C, we applied high-temperature DTA with Al_2O_3 and/or Y_2O_3-surface coated ZrO_2 crucibles from which we defined the following characteristics: congruent melting of $NbMn_2$ at $T_m(NbMn_2)$ = 1515 ± 15 °C, incongruent melting for $TaMn_2$ at $T_m(TaMn_2)$ = 1797 ± 40 °C and a practically identical melting temperature for alloy Ta40Mn60, whereas alloy NbMn displayed large primary dendrites of $NbMn_2$ and a eutectic ℓ = (Nb) + $NbMn_2$ at $T_{eut.}$ = 1493 ± 15 °C. Some of the high-temperature DTA runs are summarized in Fig. S2 and Fig. S3 of Supplementary Material. This information on the liquidus curves, complemented by SEM micrographs and EDX/WDX analyses (see Fig. 6 and Tables 4 and 5), confirmed (i) congruent melting for $NbMn_2$ (Svechnikov et al. gave T_m = 1500 °C [13]) and (ii) a rather depleted peritectic melting of $TaMn_2$ at 1797 °C, consistent with (a) the note of Savitskii et al. that $TaMn_2$ "melts above 1670 °C" [17] and (b) Svechnikov [13], who simply listed (without comment) the melting of $TaMn_2$ at 1800 °C. It should be emphasized, that in none of our samples from both systems (Nb-Mn and Ta-Mn) we observed any trace of the rhombohedral μ-phase (W_6Fe_7-type; space group $R\bar{3}m$; hex. axes: a ~ 0.47 nm, c ~ 2.58 nm). Therefore, and from the discussion (i) in Section 3.2. on the oxygen stabilized eta-phases as well as (ii) on the DFT-instability of eta-Ta_3Mn_3, (iii) the Rietveld refinements for the alloys Nb40Mn60 (as-cast after anneal at 900 °C) and Ta43Mn57 (as-cast and after anneal at 1000 °C), and (iv) the

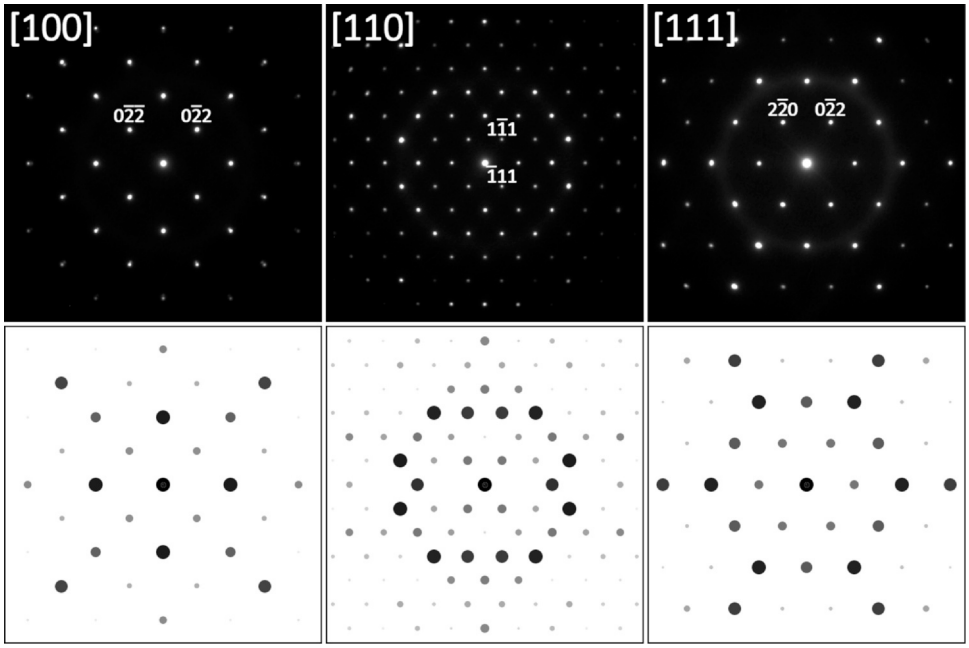

Fig. 3. SAED patterns of the cubic "TaMn" eta(η)-phase at various sample tilts (upper panel) together with results of kinematic simulation (lower panel). Weaker reflections 00k for k = 4n + 2 observed in the central horizontal line of the [110] pattern (compare the SAED and its simulation below) are caused by dynamic effects (double diffraction).

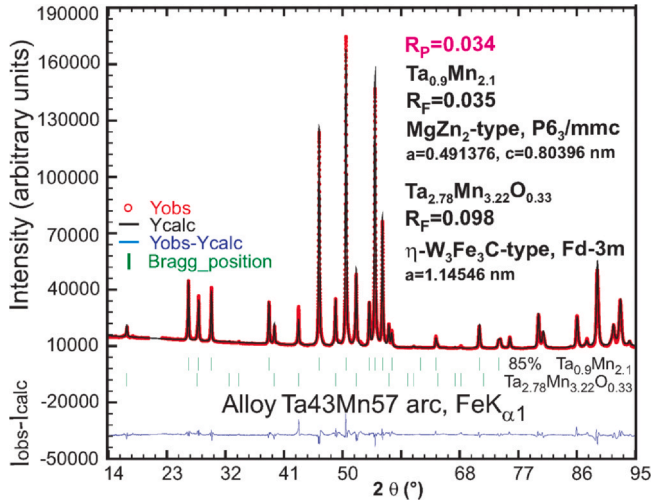

Fig. 4. Rietveld refinement of as-cast alloy Ta43Mn57. The excluded region around 2θ ≈ 22° belongs to a small peak stemming from the sample carrier foil.

solidification microstructures in Fig. 6f (Nb-Mn) and Fig. 6l (Ta-Mn), we may safely exclude the phases "NbMn" [16] and "TaMn" [18] from the corresponding binary phase diagrams.

Whilst the homogeneity regions of the two Laves phases will be treated below, the maximum solubility of Mn in (Nb) and (Ta), as derived from the cast alloys and the alloys from DTA (see also the microstructures in Fig. 6 and Tables 4 and 5) were 19.4 at% Mn in (Nb) and even 21.3 at% Mn in (Ta). In addition, it should be mentioned that for the (Nb/Ta)-rich part of the phase diagrams, DTA did not reveal any transformations from RT to the melting.

Conventional DTA (alloys sealed in quartz) and DSC (Al_2O_3-crucibles under argon) were chosen to elucidate the Mn-rich part of the phase diagrams, for which liquidus temperatures were all expected to reside below 1250 °C. Whereas the cast alloy Nb5Mn95 turned out to be fully eutectic (T_{eut} = 1220 ± 10 °C), the situation is less straightforward in the system Ta-Mn revealing an almost depleted eutectic at about 0.7 at% Ta ((δ-Mn) + $TaMn_2$ at T_{eut} = 1234 ± 10 °C) (see Fig. 6). The maximal solid solubility of (Nb) and (Ta) in δ-Mn appears to be small and is about 0.5 at% Mn for both Nb and Ta. In contrast to that, Hellawell [14] (on the basis of microstructures, TA and XPD data; but no EPMA) reported the eutectic at 3.6 at% Nb (1224 °C) and a maximum solubility of 2.4 at% Nb in δ-Mn, a value which in view of our investigations (see Fig. 6a and Table 4) seems to be exaggerated. In contrast to our findings, the data for the Ta-Mn system by Savitskii [17] exclude δ-Mn from the eutectic, which was claimed at 2.6 at% Ta at 1175 °C and formed by (γ-Mn) + $TaMn_2$. Our DTA and DSC analyses in combination with SEM-EDX/WDX on a series of alloys with 1, 2, 3, 4, 5 and 10 at% of the T-metal served to define the phase relations in the Mn-rich part of both systems Nb-Mn and Ta-Mn, which are characterized by the 4 crystal structure modifications of pure Mn and their phase transitions [12]:

$$liquid \xleftrightarrow{1246°C} \delta Mn \xleftrightarrow{1138°C} \gamma Mn \xleftrightarrow{1100°C} \beta Mn \xleftrightarrow{727°C} \alpha Mn.$$

Although the higher transition temperatures are alike, the lower two transition temperatures in the compilation from A. Dinsdale [21] (thermodynamic data of unary phases) show a discrepancy as high as about 20 °C (707 °C and 1087 °C).

EXD and WDX data inferred that for both phase diagrams the solubilities of the T-metal are below ~0.8 at% T for all modifications except for (γMn) and (αMn), the latter yielding a significant increase of its T-solubility close to its peritectoid decomposition on heating (see Fig. 6 and Tables 4 and 5), hand in hand with a pronounced increase of the (αMn) to (βMn) transformation temperature on solution (for details see the phase diagrams below in Figs. 8 and 9). It should be mentioned here, that also Savitskii et al. [17] from thermal analyses concluded a peritectoid decomposition on heating of (αMn) at ~1.5 at% Ta and 750 °C, quite similar to our DTA and EPMA data. DTA/DSC curves for selected Mn-rich alloys are presented in Fig. S4 and Fig. S5 of Supplementary Material.

3.3.1. *The homogeneity regions of the Laves phases $NbMn_2$ and $TaMn_2$*

The experimentally derived homogeneity region of the Laves phase $Nb_{1+x}Mn_{2-x}$ (62.5–73.0 at% Mn at 950 °C: −0.19 ≤x≤ 0.125) (see Fig. 7a) is fairly consistent with the reports by Drys [57] (64–69 at% Mn ≡ −0.07 ≤x ≤ 0.08 at 800 °C), Svechnikov et al. [13] (62–70 at% Mn at 1000 °C) and Blazina [58] (62–69 at% Mn at 1000°C), which was

Table 3
XPD Rietveld refinement (room temperature data) for alloys Nb40Mn60 (as-cast after anneal at 900 °C) and Ta43Mn57 (as-cast and after anneal at 1000 °C); theta range $14 \le 2\Theta \le 95°$); all structures standardized with program *Structure Tidy* [28]. Isotropic atomic displacement parameters B_{iso} in [10^2 nm^2].

Parameter/sample (at%)	Nb40Mn60; 900 °C	Ta43Mn57; arc	Ta43Mn57; 1000 °C
Profile parameters			
Number of variables	24	24	26
$R_P = \Sigma\|y_{oi}-y_{ci}\|/\Sigma\|y_{oi}\|$	0.0150	0.0348	0.0638
$R_{wP} = [\Sigma w_i\|y_{oi}-y_{ci}\|^2/\Sigma w_i\|y_{oi}\|^2]^{½}$	0.0198	0.0459	0.0871
$R_e = [(N-P+C)/\Sigma w_i y_{oi}^2)]^{½}$	0.0132	0.0085	0.0081
Laves phase	$Nb_{1.08}Mn_{1.92}$; 86 vol%	$Ta_{0.9}Mn_{2.1}$; 85 vol%	$TaMn_2$; 81 vol%
Space group, Prototype	$P6_3/mmc$, $MgZn_2$	$P6_3/mmc$, $MgZn_2$	$P6_3/mmc$, $MgZn_2$
a; c (nm)	0.489376(4); 0.800616(9)	0.491376(4); 0.803961(8)	0.48680(1); 0.79713(2)
$R_F = \Sigma\|F_o-F_c\|/\Sigma F_o$	0.0654	0.0322	0.0435
$R_I = \Sigma\|I_o-I_c\|/\Sigma I_o$	0.0826	0.0450	0.0464
Site 2*a* (0,0,0); B_{iso}	0.36(2); 0.10(2) Nb +1.90 Mn	0.20(3); 0.09(1) Ta +1.91 Mn	0.21 2 Mn
Site 4*f* (⅓,⅔,*z*); *z*; B_{iso}	0.56276(5); 0.49(3); 4 Nb	0.56381(2); 0.42(4); 3.51(1) Ta +0.49 Mn	0.56483(3); 0.41(4); 4 Ta
Site 6*h* (*x*,2*x*,¼); *x*; B_{iso}	0.1733(3); 0.57(4); 0.22(2) Nb +5.78 Mn	0.1697(1); 0.21(4); 6 Mn	0.1778(2); 0.40(6); 6 Mn
η (eta) phase #1	$Nb_{2.86}Mn_{3.14}O_{0.31}$; 14 vol%	$Ta_{2.78}Mn_{3.22}O_{0.33}$; 15 vol%	$Ta_{2.84}Mn_{3.16}O_{0.23}$; 14 vol%
Space group, Prototype	$Fd\bar{3}m$, W_3Fe_3C	$Fd\bar{3}m$, W_3Fe_3C	$Fd\bar{3}m$, W_3Fe_3C
a (nm)	1.13415(2)	1.14546(1)	1.14088(3)
$R_F = \Sigma\|F_o-F_c\|/\Sigma F_o$	0.096	0.0985	0.0980
$R_I = \Sigma\|I_o-I_c\|/\Sigma I_o$	0.114	0.0995	0.1041
Site 48*f* (*x*,⅛,⅛); *x*; B_{iso}	0.4308(2); 0.63; 42.6(3) Nb +5.4 Mn	0.4325(1); 0.55; 43.6(1) Ta +4.4 Mn	0.4288(2), 0.2; 45.4(1) Ta +2.6 Mn
Site 32*e* (*x*,*x*,*x*), *x*; B_{iso}	0.2064(3); 0.56; 3.1(2) Nb +28.9 Mn	0.2120(3); 0.12; 1.0(1) Ta +31.0 Mn	0.2038(3), 0.4; 32 Mn
Site 16*c* (0,0,0) B_{iso}	16 Mn; 0.51	16 Mn; 0.12	16 Mn; 0.4
Site 16*d* (½,½,½) B_{iso}	5.0(1) O; 0.61	5.34(8) O; 0.41	3.61(1) O; 0.55
η (eta) phase #2	no	no	$Ta_{3.01}Mn_{2.99}O_{0.13}$; 4 vol%
Space group, Prototype	–	–	$Fd\bar{3}m$, W_3Fe_3C
a (nm)	–	–	1.12859(2)
$R_F = \Sigma\|F_o-F_c\|/\Sigma F_o$	–	–	0.1020
$R_I = \Sigma\|I_o-I_c\|/\Sigma I_o$	–	–	0.1141
Site 48*f* (*x*,⅛,⅛); *x*; B_{iso}	–	–	0.4288(-); 0.2; 48 Ta
Site 32*e* (*x*,*x*,*x*), *x*; B_{iso}	–	–	0.2038(-); 0.4; 0.2 Ta +31.8 Mn
Site 16*c* (0,0,0) B_{iso}	–	–	16 Mn; 0.4
Site 16*d* (½,½,½) B_{iso}	–	–	2.05(6) O; 0.55

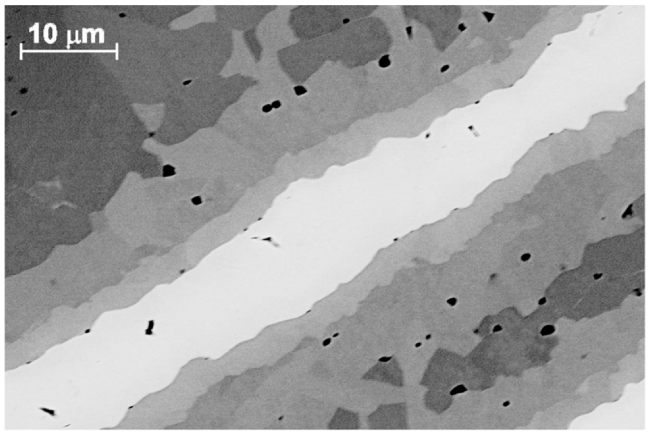

Fig. 5. SEM-BSE micrograph of HF melted alloy Ta39.8Mn60.2 (overall EDX): bright Ta99.7Mn0.3, light gray band adjacent to bright (unreacted) foil: Ta48Mn52 (Ta44.8Mn52.0O3.2 ≡ η-phase $Ta_{3-x}Mn_{3+x}O_{1-y}$ from WDX), dark gray band second next to Ta-foil: Ta46Mn54 (second η-phase) and dark Laves phase Ta40.6Mn59.4.

also used by Gupta et al. [59] for the Nb-Mn-Ni system at 1000 °C. Our study of the lattice parameters confirmed the homogeneity region obtained from EDX measurements within a small margin of ± 0.5 at% Mn (see Fig. 7a). A similarly wide homogeneity region was found from XPD for $Ta_{1+x}Mn_{2-x}$ (59.5–68.5 at% Mn for 900 °C and cast alloys: $-0.055 \le x \le 0.215$; see Fig. 7b), which is fairly consistent with the EPMA values.

At this point, it should be emphasized that both systems Nb-Mn and Ta-Mn are characterized by only one binary compound, a Laves phase with $MgZn_2$-type without any other structure modifications in the entire composition/temperature range of existence. For $NbMn_2$ this has been proven by temperature dependent XPD (4.2–300 K), X-ray SC diffractometry from 100 to 300 K and by XPD up to the melting range on quenched alloys. Fig. 7a and b display the lattice parameters of $Nb_{1+x}Mn_{2-x}$ and $Ta_{1+x}Mn_{2-x}$ as a function of composition and for a set of temperatures. For comparison, all data available in the literature are plotted (taken from [47]), although many of them lack a defined composition and can only be placed at stoichiometric TMn_2. It is interesting to see that the width of the homogeneity region $Nb_{1+x}Mn_{2-x}$ is practically invariant from 950 °C to the melting range: $-0.19 \le x \le 0.125$. Similar behavior is also encountered for $Ta_{1+x}Mn_{2-x}$.

From the energetics of point defect formation in a DFT supercell approach for the large homogeneity region of the $ZrMn_2$ Laves phase, Chen et al. [41] clearly derived that antisite occupation is more favorable than vacancy formation. Particularly the low energy for Mn at Zr sites infers a broad nonstoichiometry range toward the Mn-rich side and with increasing temperature the minimum of the free energy of the Laves phase is shifted toward Mn-richer compositions (at 32.8 at% Zr) concomitant with the occurrence of the congruent melting point not at the stoichiometric but at a slightly Mn-richer composition [41]. Similar arguments may also hold for both Laves phases $NbMn_2$ and $TaMn_2$.

3.4. DFT stability of intermetallic phases

The ab initio calculated equilibrium lattice parameters for the FIM arrangement of the various configurations of C14 Laves phases are provided below. This type of magnetic arrangement was chosen, as it shows to be the most stable (a detailed study of this topic can be found in Ref. [40]). The lattice parameters of $NbMn_2$ (a = 0.48087 nm, c = 0.79061 nm) and $TaMn_2$ (a = 0.47899 nm, c = 0.78874 nm) agree

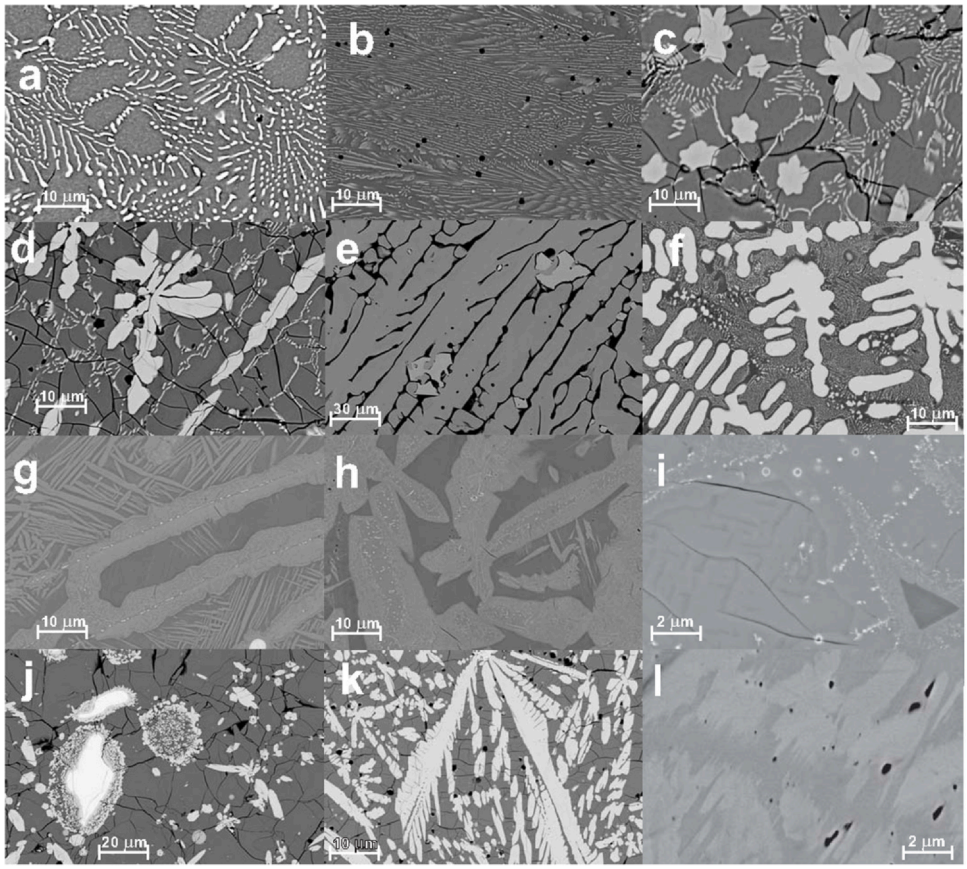

Fig. 6. SEM-BSE micrographs (EDX) for various as-cast alloys (nominal composition in at%) of the systems Nb-Mn (a to f) and Ta-Mn (g to l). (For overall EDX compositions see also Tables 4 and 5). (a) Nb4Mn96: primary dark Nb0.5Mn99.5, eutectic Nb4.8Mn95.2; (b) Nb5Mn95: eutectic Nb4.9Mn95.1; (c) Nb8Mn92: dark matrix Nb0.8Mn99.2, bright Nb27.1Mn72.9, eutectic Nb5.4Mn94.6; (d) Nb10Mn90: dark matrix Nb0.6Mn99.4; bright dendrites Nb26.0Mn74.0, eutectic; (e) Nb33.3Mn66.7: dendrites Nb34.7Mn65.3, bright particle Nb44.8Mn45.7O9.5 (WDX); (f) Nb60Mn40: bright Nb81.8Mn18.2, dark matrix Nb37.6Mn62.4, eutectic Nb53.2Mn46.8; (g) Ta1Mn99: dark Ta0.6Mn99.4, light gray Ta0.7Mn99.3, lamella-like eutectic Ta0.7Mn99.3; (h) Ta2Mn98: dark Ta0.6Mn99.4, light gray Ta0.5Mn99.5, white precip. Ta32.3Mn67.7; (i) Ta4Mn96: black Ta0.5Mn99.5, gray Ta0.43Mn99.57, eutectic Ta0.5Mn99.5, Ta-rich white particles; (j) Ta5Mn95: bright round unreacted Ta, bright angular Ta29.5Mn70.5, dark Ta0.6Mn99.4, eutectic; (k) Ta10Mn90: dark Ta0.6Mn99.4, bright dendrites Ta31.4Mn68.6; (l) Ta45Mn55 slow cool: dark Ta43.2Mn52.0O4.8, light gray Ta46.8Mn47.7O5.5.

well with the experimental data ($a = 0.48898(1)$ nm, $c = 0.79970(1)$ nm for the Nb-crystal and $a = 0.48708(1)$ nm and $c = 0.79718(1)$ nm for the Ta-crystal). In general, there is a small underestimation in case of ab initio values in the range from −1.06% (for c in $TaMn_2$) to −1.66% (both a parameters).

Consequently, the enthalpies of formation for the FIM C14 type Laves phases with respect to αMn and bcc Nb and Ta were determined as follows: − 44.29 kJ/mol.f.u. for $NbMn_2$, 157.42 kJ/mol.f.u. for Nb_2Mn, − 67.88 kJ/mol.f.u. for $TaMn_2$ and 177.28 kJ/mol.f.u. for Ta_2Mn. Our calculated value for FIM arrangement of $NbMn_2$ agrees

Table 4
EDX/WDX data (all in at%) on the constitution of the systems Nb-Mn.

Nominal composition Nb – Mn	Preparation annealing temperature	EDX overall compos.	Matrix Nb – Mn	Second phase Nb – Mn	Eutectic Nb – Mn	η-Nb-Mn (EDX) or η-Nb-Mn-O (WDX)
1–99	arc	1.0–99.0	0.6–99.4	Fine particles	–	Black holes
2–98	arc	2.0–98.0	1.5–98.5	–	–	45.3–54.7
	950 °C	2.0–98.0	0.6–99.4	–	–	44.9–54.3–0.9
3–97	arc	3.3–96.7	1.4–98.6	27.0–73.0	–	Few small
	950 °C	–	0.6–99.4	Small	–	47.0–48.6–4.4
4–96	arc; Fig. 6a	4.1–95.9	0.5–99.5	~24.2–75.8	4.8–95.2	–
	950 °C	4.0–96.0	0.6–99.4	27.5–72.5	–	44.6–55.4
	750 °C	3.9–96.1	3.3–96.7	27.2–72.8	–	44.2–55.8
5–95	arc; Fig. 6b	5.0–95.0	–	–	4.9–95.1	–
	700 °C	4.7–95.3	3.7–96.3	27.1–72.9	–	45.6–54.4
8–92	arc; Fig. 6c	9.5–90.5	0.8–99.2	27.1–72.9	5.4–94.6	47.6–52.4
	950 °C	–	0.5–99.5	27.3–72.7	Eutectic	–
10–90	arc; Fig. 6d	8.9–91.1	0.6–99.4	26.0–74.0	Eutectic	–
	950 °C	10.3–89.7	0.6–99.4	27.4–72.6	–	45.5–54.5
33.3–66.7	HF; Fig. 6e	35.3–64.7	–	34.7–65.3	–	44.8–45.7–9.5
46–54	HF	47–53	37.2–62.8	80.6–19.4	51.6–48.4	–
	920 °C	46.9–53.1	37.8–62.2	84.1–15.9	inhomog.	–
60–40	arc; Fig. 6f	58.7–41.3	37.6–62.4	81.8–18.2	53.2–46.8	–
	950 °C	58.3–41.7	36.7–63.3	83.3–16.7	inhomog.	–

Table 5
EDX/WDX data (all in at%) on the constitution of the system Ta-Mn.

Nominal composition Ta – Mn	Preparation annealing temperature	EDX overall compos.	Matrix Ta – Mn	Second phase Ta – Mn	Eutectic Ta – Mn	η-Ta-Mn (EDX) or η-Ta-Mn-O (WDX)
1–99	arc; Fig. 6g	0.8–99.2	0.6–99.4	30.6–69.4	0.7–99.3	–
2–98	arc; Fig. 6h	1.2–98.8	0.6–99.4	0.5–99.5	White precip. ~32.2–67.7	Unreacted Ta; small amount
3–97	arc	3.1–96.9	0.8–99.2	~26.4–73.6	–	46.56–53.4
	950 °C	–	0.7–99.3	~25.3–74.7	–	46.8–53.2
4–96	arc; Fig. 6i	1.3–98.7	0.5–99.5	0.4–99.6	0.5–99.5	White particles
	950 °C	0.6–99.4	0.1–99.9		–	Few whites
5–95	arc; Fig. 6j	4.2–95.8	0.6–99.4	29.5–70.5	–	Unreacted Ta; small amount
	700 °C	4.8–95.2	2.4–97.6	0.1–99.9 32.6–67.4	–	–
10–90	arc; Fig. 6k	8.4–91.6	0.6–99.4	31.4–68.6	–	–
20–80	arc	20.3–79.7	0.5–99.5	31.6–68.4	–	51.2–48.8
20–80	900 °C	25.2–74.8	0.4–99.6	31.5–68.5	–	–
45–55	arc; slow cooling; Fig. 6l	46.5–53.5	–	–	–	46.8–47.7–5.5 43.2–52.0–4.8
45–55	HF, 900 °C	43.7–56.3	40.9–59.1	85.3–14.7	–	45.9–54.1
45–55	arc; DTA	43.4–56.6	41.2–58.8	85.3–14.7	–	50.7–49.3 54.3–45.7
50–50	arc	48.6–51.4	39.4–60.6	78.7–21.3	–	–
60–40	arc; DTA	63.8–36.8	41.4–58.6	87.1–12.9 86.3–13.7	–	–

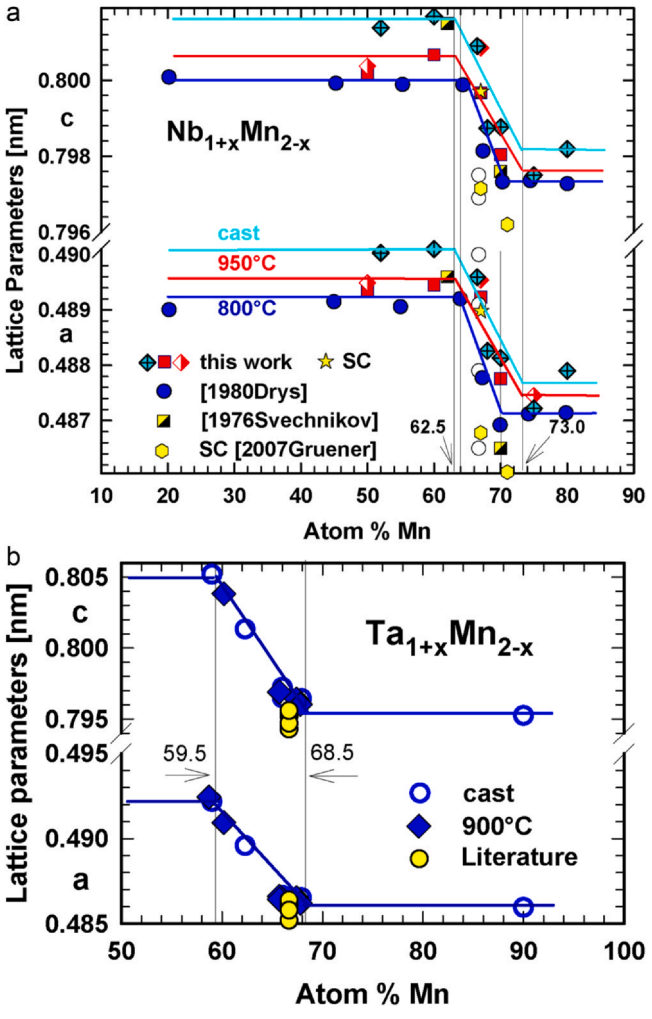

Fig. 7. (a) Lattice parameters defining the homogeneity range of the Laves phase $Nb_{1+x}Mn_{2-x}$. Open circles are various values from the literature (for data see [47]) with unspecified composition therefore plotted at $NbMn_2$. Limits of homogeneity regions are fixed to EPMA data. (b) Lattice parameters defining the homogeneity range of the Laves phase $Ta_{1+x}Mn_{2-x}$. Yellow filled circles are various values from the literature (for data see [47]) with unspecified composition, therefore plotted at $TaMn_2$. Limits of homogeneity regions are fixed to EPMA data. (For interpretation of the references to colour in this figure legend, the reader is referred to the web version of this article.)

well with both data extracted from drop isoperibolic calorimetry in a Ni bath (−45.05 ± 3.64 kJ/mol.f.u. [24]) and data calculated theoretically (−46.5 kJ/mol.f.u. by Yan et al. [24] and −42 kJ/mol.f.u. by Colinet et al. [20]). The standard enthalpy of formation measured by high-temperature direct synthesis calorimetry (−31.2 ± 8.1 kJ/mol.f.u. [23]) is somewhat lower than the results described above. The lower uncertainty extreme of the experimental heat of formation of $TaMn_2$, provided in the literature (−43.5 ± 7.5 kJ/mol.f.u. [23]) only with some caution is comparable with the calculated heat of formation with respect to αMn (−67.88 kJ/mol.f.u.). Moreover, our calculated data are much lower than those calculated by Colinet et al. (−24 kJ/mol.f.u. [20]). Nevertheless, the obtained negative values confirm thermodynamic stability of the $NbMn_2$ and $TaMn_2$ Laves phases. The calculated energies of formation of four above-mentioned configurations of the C14 Laves phase were used to evaluate the thermodynamic description of end-members in terms of the sublattice model. These data were supplemented by ab initio calculated energies of formation from the literature concerning the Mn_2Mn [60], Nb_2Nb [61] and Ta_2Ta [61] configuration of the C14 Laves phase.

The DFT calculations were also used to evaluate the stability of the cubic eta-phase (Ta_3Mn_3; space group $Fd\bar{3}m$ (#227; origin at center); Ta in 48*f* sites, Mn in sites 32*e* + 16*c*) and the influence of O on it. For oxygen, one atom was accommodated to the sublattice 8*a* or 8*b* ($Ta_{48}Mn_{48}O$) or eight atoms to the sublattice 16*d* ($Ta_{48}Mn_{48}O_8$). The calculations showed that the eta-phase Ta_3Mn_3 is stabilized compared to the SER states by −10.02 kJ/mol at., which is a lower value than that calculated by Colinet et al. (−18 kJ/mol.f.u. ≡ −9 kJ/mol at. [20]). However, taking C14-$TaMn_2$ and pure bcc Ta as reference states, the eta-phase becomes unstable by 6.95 kJ/mol at. This explains why this phase has not been observed in the Ta-Mn binary system. Inserting one atom of O in the 8*a* site ($Ta_{48}Mn_{48}O$) resulted in the energy of formation of − 9.94 kJ/mol at. with respect to SER states. Although this value suggests a stabilizing influence compared to SER states, it is even smaller than the value for Ta_3Mn_3, indicating that this structure will be also unstable when the Laves phase is present (by 6.85 kJ/mol at. with respect to the weighted ratio of bcc Ta, O_2 and C14-$TaMn_2$). Furthermore, we also investigated the energy of formation of eta-phase containing one O atom in the 8*b* sublattice with respect to the SER states, which resulted in the value of −14.97 kJ/mol at. This value proves that the O atoms prefer the 8*b* sublattice to 8*a* and makes the structure only slightly unstable with respect to the weighted ratio of bcc Ta, O_2 and C14-$TaMn_2$ by 1.83 kJ/mol at. Hence, it can be suggested that this structure could become stable at higher temperatures. On the other hand, the addition of 8 atoms of O to the 16*d* sublattice

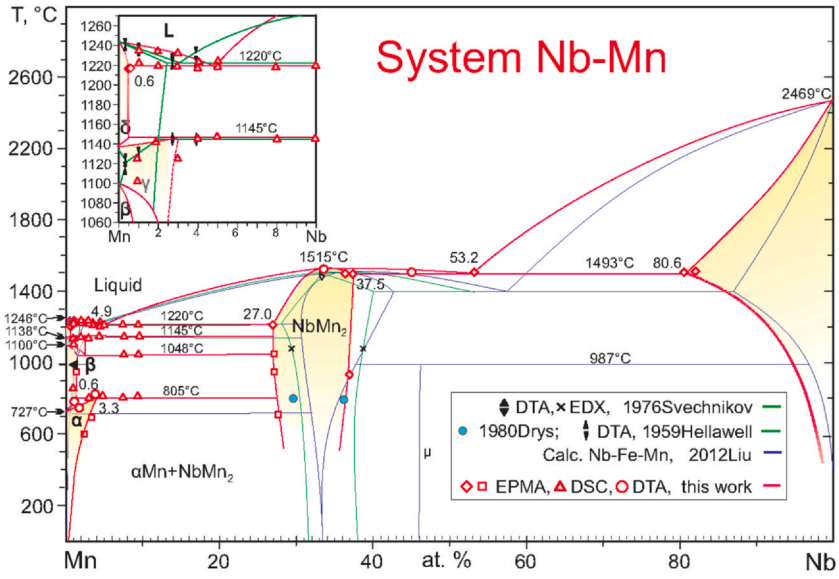

Fig. 8. Phase diagram of the binary system Nb-Mn. Red symbols denote EPMA and DTA/DSC data and red lines denote this work. For comparison data from literature are included (listed in the legend). Single-phase solid regions are shaded in yellow. (For interpretation of the references to colour in this figure legend, the reader is referred to the web version of this article.)

($Ta_{48}Mn_{48}O_8$) resulted in massive stabilization. The most stable of the studied configurations of this structure was stabilized even by − 38.01 kJ/mol at. with respect to SER states, which subsequently provides stability in presence of C14-$TaMn_2$. These results confirm the experimental findings of the O stabilization of the eta-phase and the O preference for sublattices in the sequence 16*d* > 8*b* > 8*a*. Based on the experimental data we would expect, that the situation is quite similar for η-$Nb_3Mn_3O_{1-y}$ leaving $Nb_{1+x}Mn_{2-x}$ the only compound in the binary Nb-Mn system.

Due to the lack of phase diagram information on the Ta-Mn-O system, we have chosen here two types of reference states: (i) SER states or (ii) bcc Ta, C14-$TaMn_2$ and O_2. However, for a correct determination of the overall stability of η-Ta_3Mn_3O (and η-Nb_3Mn_3O), phase relations need to be known among all binary and ternary oxide phases. Although the eta-oxides are close to the Nb(Ta)-Mn binary, the influence of the boundary phases in the Nb(Ta)-Mn-O systems could further reduce their degree of stability. Consequently, the topic of the Mn-based Laves and eta-phases (their stability, arrangement and magnetism) is much more complex and deserves more attention, which will be paid to it in the forthcoming publication [40], where, among other things, the stabilization effect of O in the eta-phase will be discussed in detail.

3.5. Thermodynamic modeling of the systems Nb-Mn and Ta-Mn

The experimental phase diagrams of the systems Nb-Mn and Ta-Mn, as presented in Figs. 8 and 9, form the basis for our thermodynamic modeling backed by the DFT calculated energies of formation of different configurations of the Laves phases $NbMn_2$ and $TaMn_2$ (Chapter 3.4). Thermodynamic data for pure elements were taken from [21]. Parameters for CAPHAD calculations of phase diagrams of Nb-Mn and Ta-Mn systems as the result of modeling are given in Table 6 and phase diagrams are drawn in Fig. 10 and Fig. 11. A comparison of the experimentally derived and thermodynamically calculated details on the invariant equilibria, as presented in Tables S1 and S2 in Supplementary Material, shows a convincing

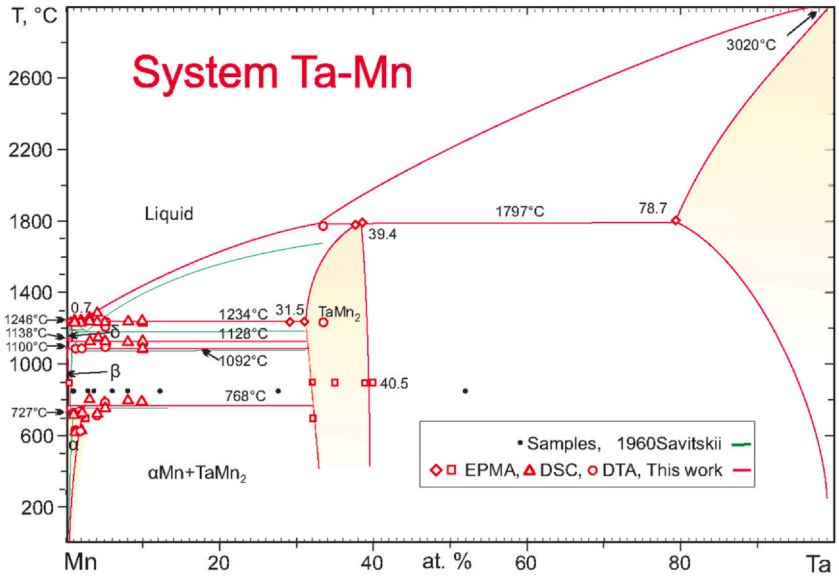

Fig. 9. Phase diagram of the binary system Ta-Mn. Red symbols denote EPMA and DTA/DSC data and red lines denote this work. For comparison data from literature are included (listed in the legend). Single-phase solid regions are shaded in yellow. (For interpretation of the references to colour in this figure legend, the reader is referred to the web version of this article.)

Table 6
Parameters for calculations of phase equilibria in the Nb-Mn and Ta-Mn systems.

Mn-Nb phase diagram
PHASE LIQUID (MN,NB)
$^{\circ}L_{Liquid}$(MN,NB) = −12100
$^{1}L_{Liquid}$(MN,NB) = −6800
PHASE BCC_A2 (MN,NB)(VA)
$^{\circ}L_{BCC\_A2}$(MN,NB:VA) = 11300
$^{1}L_{BCC\_A2}$(MN,NB:VA) = −10200
TC_{BCC_A2}(MN:VA) = 580
BM_{BCC_A2}(MN:VA) = 0.27
PHASE FCC_A1 (MN,NB)(VA)
$^{\circ}L_{FCC\_A1}$(MN,NB:VA) = −15200
TC_{FCC_A1}(MN:VA) = 540
BM_{FCC_A1}(MN:VA) = 0.62
PHASE CUB_A13 (MN,NB)(VA)
$^{\circ}L_{CUB\_A13}$(MN,NB:VA) = −18500
PHASE CBCC_A12 (MN,NB)(VA)
$^{\circ}L_{CBCC\_A12}$(MN,NB:VA) = −30750
TC_{CBCC_A12}(MN:VA) = 95
BM_{CBCC_A12}(MN:VA) = 0.22
PHASE MN2NB (MN,NB)(MN,NB)
$^{\circ}G_{MN2NB}$(MN:MN) = 3*GHSERMN + 23478 + 5*T
$^{\circ}G_{MN2NB}$(MN:NB) = 2*GHSERMN + GHSERNB-44290 + 5.02*T
$^{\circ}G_{MN2NB}$(NB:MN) = 2*GHSERNB + GHSERMN + 157421 + 9*T
$^{\circ}G_{MN2NB}$(NB:NB) = 3*GHSERNB + 46099
$^{\circ}L_{MN2NB}$(MN,NB:NB) = 15000
$^{\circ}L_{MN2NB}$(MN,NB:MN) = −15000
$^{\circ}L_{MN2NB}$(NB:MN,NB) = 30000
$^{\circ}L_{MN2NB}$(MN:MN,NB) = −35000
Mn-Ta phase diagram
PHASE LIQUID (MN,TA)
$^{\circ}L_{Liquid}$(MN,TA) = 6000
$^{1}L_{Liquid}$(MN,TA) = −6200
PHASE BCC_A2 (MN,TA)(VA)
$^{\circ}L_{BCC\_A2}$(MN,TA:VA) = 21600
$^{1}L_{BCC\_A2}$(MN,TA:VA) = 800
PHASE FCC_A1 (MN,TA)(VA)
$^{\circ}L_{FCC\_A1}$(MN,TA:VA) = −1650
$^{1}L_{FCC\_A1}$(MN,TA:VA) = 9000
PHASE CUB_A13 (MN,TA)(VA)
$^{\circ}L_{CUB\_A13}$(MN,TA:VA) = 19800
$^{1}L_{CUB\_A13}$(MN,TA:VA) = 5000
PHASE CBCC_A12 (MN,TA)(VA)
$^{\circ}L_{CBCC\_A12}$(MN,TA:VA) = 0
$^{1}L_{CBCC\_A12}$(MN,TA:VA) = −13500
PHASE MN2TA (MN,TA)(MN,TA)
$^{\circ}G_{MN2TA}$(MN:MN) = 3*GHSERMN + 23478 + 5*T
$^{\circ}G_{MN2TA}$(MN:TA) = 2*GHSERMN + GHSERTA - 67884 + 21.5*T
$^{\circ}G_{MN2TA}$(TA:MN) = 2*GHSERTA + GHSERMN + 177283 + 113*T
$^{\circ}G_{MN2TA}$(TA:TA) = 3*GHSERTA + 28038 + 20*T
$^{\circ}L_{MN2TA}$(MN,TA:TA) = 0
$^{\circ}L_{MN2TA}$(MN,TA:MN) = −4550
$^{\circ}L_{MN2TA}$(TA:MN,TA) = −4550
$^{\circ}L_{MN2TA}$(MN:MN,TA) = 0

agreement; in addition also the databases (tdb files) for the calculation of the phase diagrams of both systems are listed in Supplementary Material (Tables S3 and S4).

4. Physical properties of the Laves phases $NbMn_2$ and $TaMn_2$

As usual for samples within a homogeneity region, we have to emphasize that certain physical properties as well as their temperature dependencies are highly variable and sample dependent. This section covers only the single-phase compounds $NbMn_2$ (Nb34Mn66 in at%) and $TaMn_2$ (Ta33Mn67) close to their stoichiometric 1:2 composition.

4.1. Susceptibility

The temperature dependent dc magnetic susceptibility, X(T) = M/H(T), of single-phase $NbMn_2$ (Nb34Mn66) and $TaMn_2$ (Ta33Mn67) shown in Fig. 12 was measured with an applied field of 3 T and reveals paramagnetic behavior of both compounds. Considering the obviously dominant, weakly temperature dependent Pauli paramagnetic component, we analyze these data in terms of a Pauli component, $\chi_P(T) = \chi_0(1 - aT^2)$, where a is the leading coefficient of a Sommerfeld expansion, superimposed by a Curie-Weiss component, $\chi_{CW}(T) = C/(T - \theta_p)$ due to paramagnetic impurities, which are expected to arise from Mn-atoms located at Nb- or Ta-sites [62]. The corresponding fits of the measured magnetic susceptibilities $\chi_{exp}(T) = \chi_P(T) + \chi_{CW}(T)$ are shown as solid lines. For the Pauli components of the magnetic susceptibility we obtain $\chi_0 = 1.73 \times 10^{-3}$ emu/mol and $a = 3.05 \times 10^{-6}$ K^{-2} for $NbMn_2$ as well as $\chi_0 = 1.37 \times 10^{-3}$ emu/mol and $a = 2.44 \times 10^{-6}$ K^{-2} for $TaMn_2$. The Curie-Weiss components are characterized by a rather small Curie constant C = 0.0032 emuK/mol and paramagnetic Weiss temperature θ_p = −2.3 K for $NbMn_2$ (thus, indicating a relatively small number of localized Mn-moments, i.e. a small fraction of Nb-sites being occupied by Mn-atoms) and roughly a factor seven larger C = 0.021 emuK/mol and θ_p = −20 K for $TaMn_2$ (i.e., suggesting a correspondingly larger fraction of Ta-sites being occupied by Mn-atoms in this sample). We emphasize, that in particular the magnitudes of the Curie-Weiss components of the magnetic susceptibility of these Laves phase compounds are highly variable and sample dependent, when varying the stoichiometry within their homogeneity region.

The insert of Fig. 12 (upper panel) displays the dc magnetic susceptibility of a $NbMn_2$ sample containing η-phase and Fig. 12 (lower panel) displays ac susceptibility data of $NbMn_2$ and $TaMn_2$ samples with an intentionally higher fraction of eta-phases $Nb_3Mn_3O_{1-y}$ and $Ta_3Mn_3O_{1-y}$, respectively. These data reveal a pronounced ferromagnetic contribution of the $Nb_3Mn_3O_{1-y}$ and $Ta_3Mn_3O_{1-y}$ impurity phases, both with a Curie temperature $T_C \sim 77$ K. The latter contribution has been verified, at least qualitatively, to scale with the relative fraction of the η-phase.

4.2. Specific heat

Specific heat data of $NbMn_2$ (Nb34Mn66) and $TaMn_2$ (Ta33Mn67), presented as C/T vs T in Fig. 13, reveal moderately enhanced Sommerfeld-like, roughly T-linear, specific contributions with $\gamma \sim 33(1)$ mJ/mol.K^2 for $NbMn_2$ and $\gamma \sim 28(1)$ mJ/mol.K^2 for $TaMn_2$ at temperatures below 10 K. The relative magnitudes of these two Sommerfeld coefficients conform reasonably well with the relative magnitudes of the corresponding Pauli susceptibilities χ_0 of $NbMn_2$ and $TaMn_2$ (see above). There are moderate, but nonetheless obvious deviations from the expected $\gamma T + \beta T^3$ behavior of simple paramagnetic metals: in C/T vs. T of $TaMn_2$ there is a small hump centered at around 4–5 K and for $NbMn_2$ a rather moderate low-temperature upturn in C/T is observed. These behaviors obviously relate to magnetic contributions due to weakly interacting paramagnetic moments (i.e., due to the Curie-Weiss-type paramagnetic susceptibility component discussed above), which we attribute to anti-site Mn-atoms at Nb(Ta)-sites. The latter proposal is motivated by a strong increase of such magnetic low-temperature contributions for Mn-richer samples formed within the homogeneity region of these Laves phases and will be analyzed in a separate paper. The admixture of magnetic contributions at low temperatures impedes an unambiguous evaluation of the low-temperature Debye temperature of these compounds for which we can provide only rough estimates of about 430 K for $NbMn_2$ and 370 K for $TaMn_2$, which we obtain from the analysis of the phonon contributions in a $(C - \gamma T)/T^3$ versus log(4.93 T) plot, shown as an insert in Fig. 13. The corresponding Debye functions representing the acoustic phonon spectral weight are displayed as solid lines in this graph. The observed excess contributions at lowest temperatures up to the first local minimum of the experimental data in this graph (at T ~ 7 K for $NbMn_2$ and T ~ 10 K for $TaMn_2$) are attributed to primarily originate from interactions among diluted localized magnetic moments, whereas excess

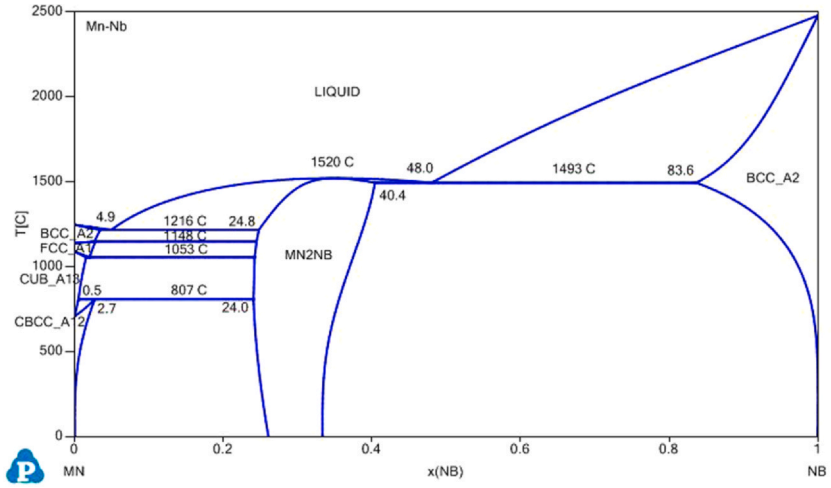

Fig. 10. CALPHAD phase diagram of the system Nb-Mn presenting phase regions and invariant temperatures.

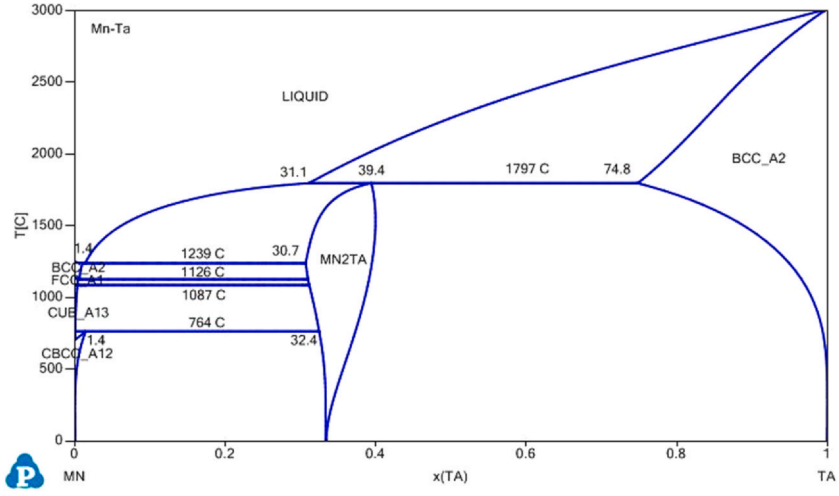

Fig. 11. CALPHAD phase diagram of the system Ta-Mn presenting phase regions and invariant temperatures.

contributions observed above the local minima of the experimental data are due to the obviously expected phonon contributions related to the optical phonon spectral weight. The corresponding local maxima of the experimental data, thus, refer to distinct maxima in the optical phonon spectral weight [63,64] at around $\theta_E \sim 120$ K for $NbMn_2$ and $\theta_E \sim 160$ K for $TaMn_2$.

As far as the $\theta_D = 430$ K of $NbMn_2$ is concerned, the value derived from C/T vs T fits quite well to an analysis of atom vibrations extracted from the atom displacement parameters as a function of temperature ($\theta_D = 398$ K, from temperature dependent X-ray single crystal data; see Fig. 14). Similarly, the extracted Sommerfeld constant $\gamma \sim 33$ mJ/mol.K^2 might appear somewhat higher than the DFT value of $\gamma = 10.5$ mJ/mol.K^2 derived from DFT calculations [24].

4.3. Electrical resistivity

The electrical resistivities, $\rho(T)$, as presented in Fig. 15 for both compounds $NbMn_2$ (Nb34Mn66 at%) and $TaMn_2$ (Ta33Mn67 at%), display metallic behavior in the measured temperature range (4–300 K), which (considering the above magnetic susceptibility and specific heat results) are expected to essentially result from electron-defect, electron-phonon, electron-electron and electron-paramagnon scattering. In order to qualitatively analyze these experimental data, we assign a tentative estimate of the electron-defect and electron-phonon scattering contributions as $\rho(T) = \rho_0 + \rho_{BG}(T)$ (see Eq. (7); BG is the Bloch-Grüneisen relation), displayed as dashed lines in Fig. 15, where we make use of the above estimates of the Debye temperatures of these compounds from their specific heat data.

$$\rho(T) = \rho_0 + 4\ \Re\left(\frac{T}{\theta_D}\right)^5 \int_0^{\theta_D/T} \frac{z^5}{(e^z - 1)\cdot(1 - e^{-z})} dz \quad \text{with } z = \frac{\hbar_\omega}{k_B T} \tag{7}$$

θ_D stands for the Debye temperature and $\Re$ is a temperature independent electron-phonon interaction constant. Subtracting these estimated $\rho_0 + \rho_{BG}(T)$ contributions from the totally measured electrical resistivities, $\rho(T)$, we obtain a rough estimate of electron-electron and electron-paramagnon scattering contributions, $\Delta\rho(T) = \rho(T) - [\rho_0 + \rho_{BG}(T)]$, displayed in Fig. 16, which appear to be rather similar for $NbMn_2$ and $TaMn_2$ despite of their almost one order of magnitude different residual resistivity values of $\rho_0 = 26$ μΩcm versus 220 μΩcm, respectively. When analyzing the temperature dependence of $\Delta\rho(T)$ for $T < 35$ K by a simple power law fit $\Delta\rho(T) = aT^n$, we obtain exponents n close to three, i.e. clearly different values from a trivially expected $\rho_{el}(T) \propto T^2$. The initially larger contribution $\Delta\rho(T)$ of $TaMn_2$, as compared to $NbMn_2$, obviously relates to its larger Curie-Weiss component of the magnetic susceptibility (see above). We have

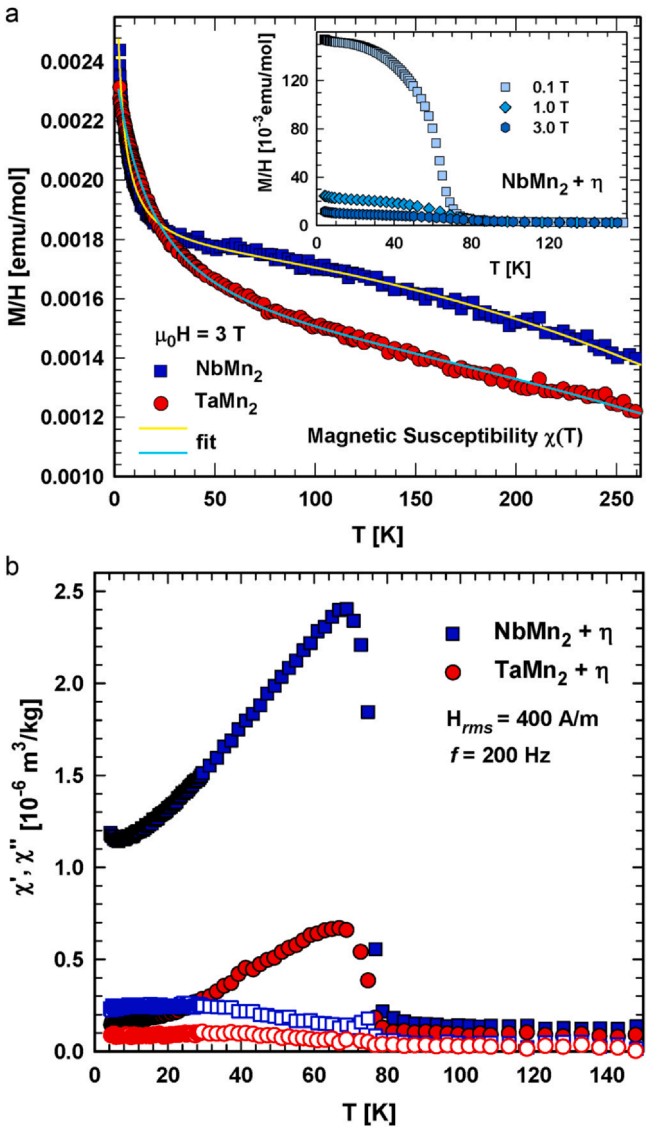

Fig. 12. Upper panel: Temperature dependent dc magnetic susceptibility, $\chi(T) = M/H(T)$, of single-phase $NbMn_2$ (Nb34Mn66) and $TaMn_2$ (Ta33Mn67) in an applied field of 3 T. Solid lines are combined Curie-Weiss plus Pauli susceptibility fits (see text); insert: magnetic susceptibility of a sample of $NbMn_2$ containing η-phase $Nb_3Mn_3O_{1-y}$, measured at various dc magnetic fields as labeled. Lower panel: AC susceptibility χ' (filled symbols) and χ'' (open symbols) of samples $NbMn_2$ and $TaMn_2$ with an intentionally higher fraction of eta-phase $Nb_3Mn_3O_{1-y}$ and $Ta_3Mn_3O_{1-y}$, respectively.

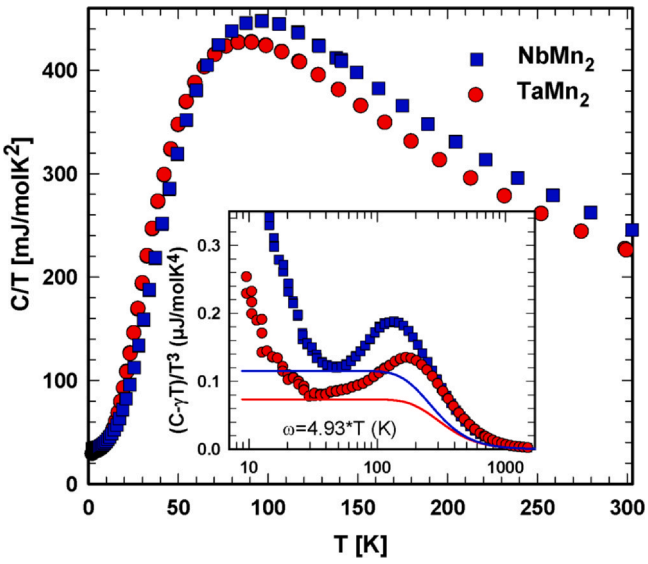

Fig. 13. Specific heat data C/T vs. T for $NbMn_2$ (Nb34Mn66) and $TaMn_2$ (Ta33Mn67). Insert: plot of $(C - \gamma T)/T^3$ versus log(4.93 T) where experimental data are shown as symbols and corresponding estimates of the contribution of acoustic phonon branches are displayed by Debye functions as solid lines.

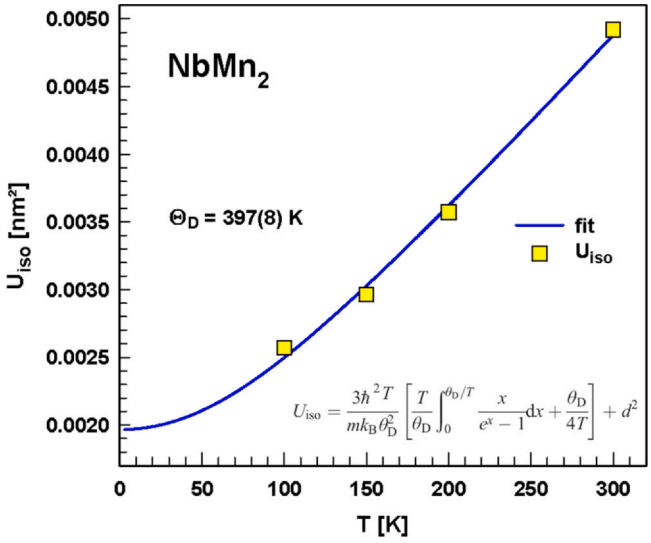

Fig. 14. Atom displacement factors U_{iso} versus temperature for $NbMn_2$. The blue line is a least squares fit to the Debye vibrations according to the equation given in the graph. (For interpretation of the references to colour in this figure legend, the reader is referred to the web version of this article.)

to emphasize that the magnitude of the residual resistivity as well as the low-temperature power law exponent n of these Laves phase compounds are highly variable and sample dependent, in particular when varying the stoichiometry of these compounds within the homogeneity region.

4.4. Hardness and mechanical properties

The results of the hardness measurements are presented in Fig. 17. For $NbMn_2$ (Nb36Mn64 at%) as well as for $TaMn_2$ (Ta35Mn65 at%), static and dynamic (MI) hardness is decreasing with increasing loads and level out for $F \geq 1$ N resulting for $NbMn_2$ in a static $HV_{0.1} = 823$ and in a dynamic hardness (MI) value $HV_{0.1} = 735$. For $TaMn_2$ the respective values are slightly higher with $HV_{0.1}(stat) = 900$ and $HV_{0.1}(dyn) = 815$, respectively. Dynamic hardness values are lower than the static ones, which is not unusual, because in case of the static hardness measurement the imprint shrinks as soon as the load is withdrawn, whereas the dynamic hardness is evaluated during the impression. The dynamic hardness values, measured with the nanoindenter, with $HV_{0.01} = 724.7 \pm 46.6$ for $NbMn_2$ and $HV_{0.01} = 815.9 \pm 73.3$ for $TaMn_2$ are in good agreement with those measured with the microindenter (for all hardness data, also converted into GPa see Table 8). Whereas Savitskii's hardness data for $TaMn_2$ (720 kg/mm^2 at a load of 100 g [17]) are close to our values, Svechnikov et al. [13] arrived at slightly higher values (at a 100 g load): 1020 kg/mm^2 for $TaMn_2$ and 1040–1250 kg/mm^2 across the homogeneity region of $NbMn_2$.

The Young's moduli, E, dependent on the applied force, and evaluated with the Poisson's ratio of $\nu = 0.36$ (from DFT calculations for $NbMn_2$ [32]), are displayed in Fig. 18. E is load dependent and decreasing with increasing load, flattening out for forces $F \geq 1.5$ N and reaching $E = 203$ GPa for $NbMn_2$ and $E = 232$ GPa for $TaMn_2$. Both values are in very good agreement with $E = 203.4 \pm 15$ GPa and

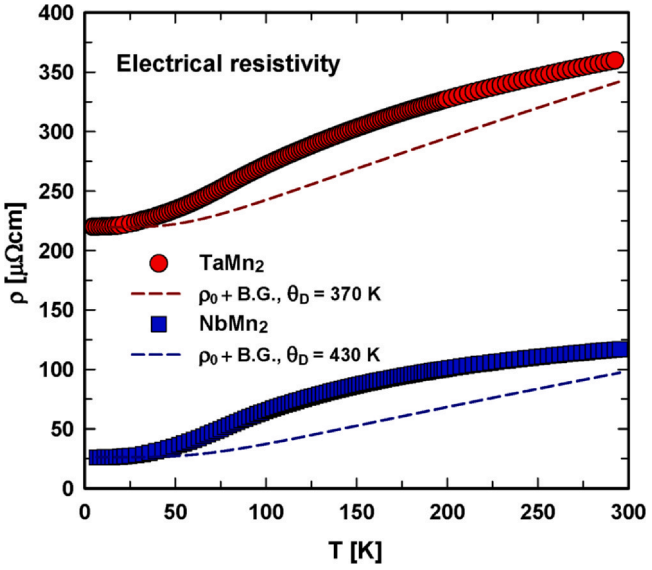

Fig. 15. Temperature dependent electrical resistivity, ρ(T), of $NbMn_2$ (Nb34Mn66) and $TaMn_2$ (Ta33Mn67). Solid lines indicate tentatively assigned residual resistivity plus Bloch-Grüneisen electron-phonon scattering contributions (see text).

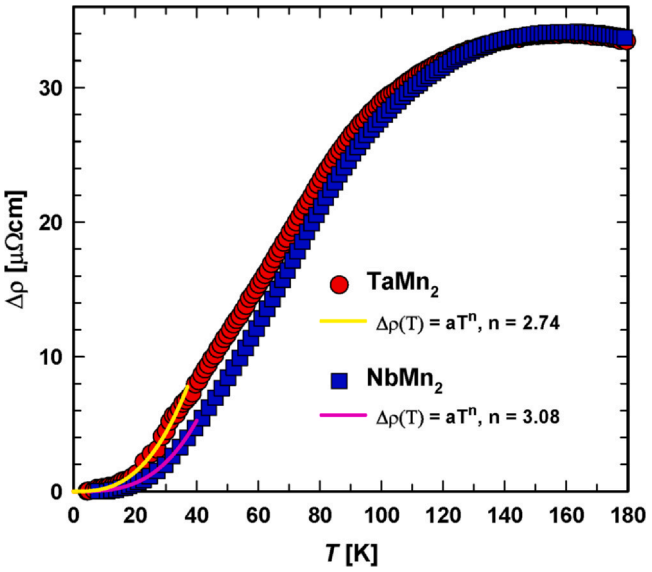

Fig. 16. Estimated resistivity contributions, Δρ(T), due to electron-electron and electron-paramagnon scattering obtained by subtracting other contributions as tentatively indicated by dashed lines in Fig. 15. Solid lines are power law fits to the low-temperature behavior (see text).

E = 233.9 ± 16 GPa, respectively, evaluated from the nanoindenter measurements as well as with the DFT value E_H = 197 calculated for $NbMn_2$ [32] (for details see Table 7).

For the calculations of the bulk modulus, B, and the shear modulus, G, the following equations were applied:

$$B = \frac{E}{3(1-2\nu)},\quad G = \frac{E}{2(\nu+1)}. \tag{8}$$

The results for $TaMn_2$, B ~ 277 GPa, G ~ 86 GPa, are slightly higher than those for $NbMn_2$ with B ~ 242 GPa, G ~ 75 GPa (for details see Table 7). This bulk modulus value for $NbMn_2$ is fairly consistent with the values obtained from DFT calculations of a previous work of the

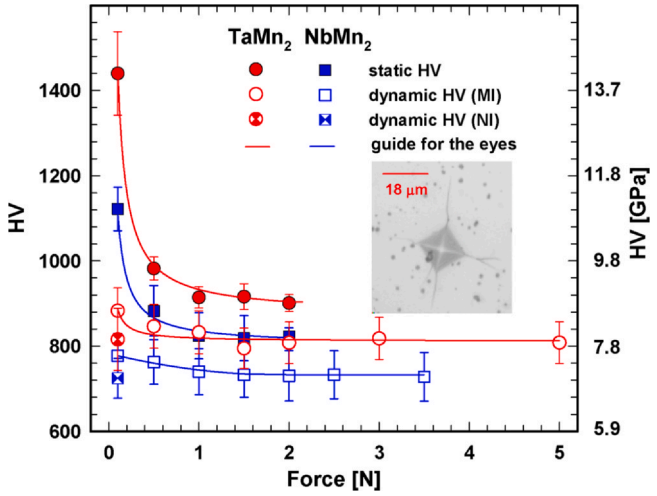

Fig. 17. Static and dynamic (MI) hardness, HV, of $NbMn_2$ and $TaMn_2$ vs. load. The solid lines are guides for the eyes. The scale on the y-axis (right) transfers HV values to GPa. Insert: Imprint with crack propagation lines.

authors [24] with B ~ 250 GPa for the paramagnetic and B = 200–220 GPa for ferromagnetic and antiferromagnetic $NbMn_2$.

According to the criterion of Pugh [65] that materials with G/B < 1.75 are brittle, both compounds $NbMn_2$ and $TaMn_2$ with G/B = 0.309 classify as brittle.

For isotropic compounds, it is possible to determine the Debye temperature, θ_D from the sound velocity, using Anderson's Eq. (9) [66]:

$$\theta_D = \frac{h}{k_B}\left(\frac{3nLd}{4M\pi}\right)^{1/3} v_m, \tag{9}$$

where h is the Plank's constant, k_B is the Boltzmann's constant, L is Loschmidt's number, d is the density, M is the molecular weight, and n is the number of atoms. The mean sound velocity v_m follows from relations (10) [66]:

$$v_m = \left[\frac{1}{3}\left(\frac{2}{v_T^3}+\frac{1}{v_L^3}\right)\right]^{-1/3}$$
$$\text{with } v_L = \left(\frac{3B+4G}{3d}\right)^{1/2}$$
$$\text{and } v_T = \left(\frac{G}{d}\right)^{1/2} \tag{10}$$

Whereas for $NbMn_2$ Debye temperatures of θ_D = 423 K (MI) and θ_D = 424 K (NI), were calculated, we arrive for $TaMn_2$ at somewhat smaller values of θ_D = 378 K (MI) and θ_D = 377 K (NI), respectively.

Fracture toughness is a measure of the resistance of a material to crack propagation. As can be seen in the insert of Fig. 17, cracks were produced from the imprint, from which we calculate the indentation fracture toughness K_{IC} using Eq. (11):

$$K_{IC} = \beta \left(\frac{E}{HV}\right)^{1/2}\frac{F}{c^{3/2}}, \tag{11}$$

where E is the Young's modulus, HV is the hardness, F is the indentation load, c is the radial crack length from the center of the Vickers indentation and β is a function of the indenter angle, which for Vickers indentation is β = 0.016(4). The indentation fracture toughness usually is substituted for fracture toughness in case of brittle materials, or for samples not big enough to qualify for the standard methods to determine fracture toughness (like the Chevron Notched Flexure Specimen method, the Single-Edge Precracked Beam method or the sharp 'V' notch beam method). The results are

Table 7
Elastic constants c_{ij} for $NbMn_2$ (all in GPa; density d = 8.15 g/cm^3) and for $TaMn_2$ (d = 11.86 g/cm^3; c_{66} = (c_{11}-c_{12})/2); shear modulus G; bulk modulus B; Young's modulus E; subscripts V, R, H refer to Voigt, Reuss limits and Hill average; Poisson's ratio ν; mean sound velocity $\bar{v}_m$ in ms^{-1}; Debye temperature θ_D in K; references (t.w. = this work); values in cursive script were completed in this work from the C_{ij} matrix of the author [24,32].

c_{11} E (010)	c_{12}	c_{13}	c_{33} E (001)	c_{44}	G_V	G_R	G_H	B_V	B_R	B_H	E_V	E_R	E_H	ν	$\bar{v}_m$	θ_D	Ref.
$NbMn_2$[a]																	
346	218	180	384	68	*73*	*71*	*72*	*248*	*248*	248	*200*	*194*	*197*	0.36	*3214*	*410*	[24,32]
341#				75#			75#			242#			203#		3407#	423#	t.w.
$TaMn_2$																	
391#				86#			86#			277#			233#	0.36	3025#	378#	t.w.

[a] For paramagnetic C14-type; # data extracted from microindentation and nanoindentation measurements.

Table 8
Properties (static hardness ($HV_{0.1}$(stat.) in GPa), dynamic hardness via microindenter ($HV_{0.1}$ (MI) in GPa), dynamic hardness via nanoindenter ($HV_{0.01}$ (NI) in GPa), Bulk modulus B (DFT) in GPa, Debye temperature calculated with E (MI) (θ_D(MI)) in K, fracture resistance, (K_{IC}) in MPam$^{1/2}$, Debye temperature calculated with E (NI) (θ_D (MI)) in K, Debye temperature via Mukherjee-fit (θ_D(MUK)) in K, Einstein temperature via Mukherjee-fit (θ_E) in K, thermal expansion coefficient (α)*10^{-6} in K^{-1}.

Properties	$NbMn_2$	$TaMn_2$	Ref.
$HV_{0.1}$ (stat.)	823 (9.2)	900 (10.1)	tw.
$HV_{0.1}$ (MI)	735 (7.5)	815 (7.9)	tw.
$HV_{0.01}$ (NI)	724.7 (7.1)	815.9 (8.0)	tw.
HV	–	730	[17]
HV	1040–1250	1020	[13]
B (DFT), paramagnetic	250	–	[24]
B (DFT), ferromagnetic	200–220	–	[24]
B (DFT), antiferromagnetic	220	–	[24]
θ_D (C_p)	~430	~370	tw.
θ_D (U_{ij})	397	–	tw.
θ_D (therm. exp.)	413	–	tw.
θ_E (therm. exp.)	87	–	tw.
θ_E (C_p)	~166	~135	tw.
α	10.9	–	tw.
K_{IC}	1.1	1.5	tw.

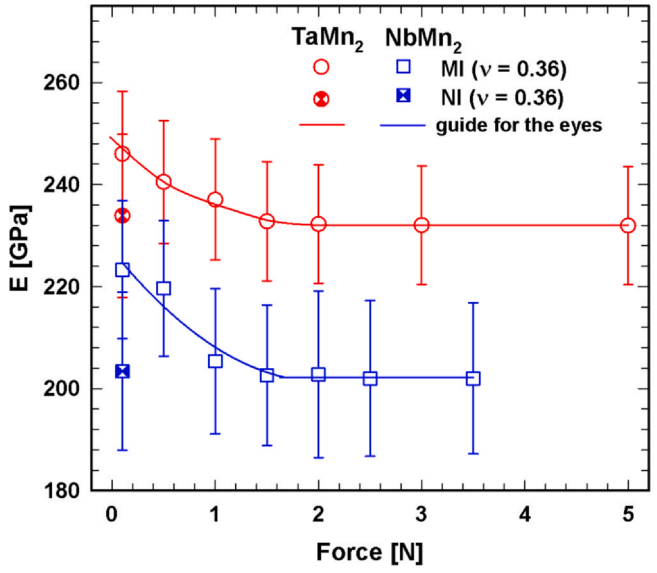

Fig. 18. Elastic modulus, E, vs. load for $NbMn_2$ and $TaMn_2$. The solid lines are guides for the eye.

almost alike to those of measured fracture toughness data. Evaluating many crack lengths for various loads from static and dynamic hardness imprints, yields a K_{IC} = 1.1 ± 0.5 MPa m$^{1/2}$ for $NbMn_2$ and K_{IC} = 1.5 ± 0.2 MPa m$^{1/2}$ for $TaMn_2$. From $\sigma \approx E^{1/2}$ a rough estimation of the fracture strength can be derived, which reveals for $NbMn_2$ $\sigma \approx 14$ GPa$^{1/2}$ and for $TaMn_2$ $\sigma \approx 15$ GPa$^{1/2}$.

Thermal expansion of $NbMn_2$ was measured in the temperature range of 4.2–300 K (Fig. 19). The corresponding $\frac{\Delta\ell}{\ell(T_0)}$ vs. T curve

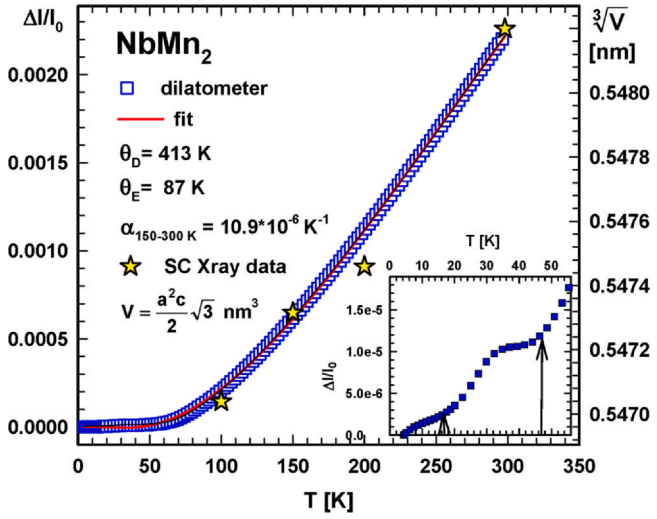

Fig. 19. Temperature dependent dilatometric thermal expansion of $NbMn_2$. Stars represent SC X-ray data from Table 2. For the fit see text.

shows a strictly linear behavior above 150 K. Consequently, a linear fit in the temperature range of 150–300 K reveals a thermal expansion coefficient $\alpha = 10.9 \times 10^{-6}$ K^{-1}. Besides extracting the thermal expansion coefficient, the semi-classical treatment by Mukherjee et al. [67] was applied to analyze the thermal expansion as a function of temperature, taking into account the Debye model for acoustic phonons and the Einstein approximation for the optical modes.

The length change $\frac{\Delta\ell}{\ell(T_0)}$ is given by:

$$\frac{\Delta\ell}{\ell(T_0)} = \frac{\langle x\rangle_T - \langle x\rangle_{T_0}}{x_0}, \quad \langle x\rangle_T = \frac{\delta}{2}T^2 + \frac{3g}{4c^2}[\varepsilon - G\varepsilon^2 - F\varepsilon^3]$$

$$\varepsilon = \left\{\left(\frac{3}{p}\right)3k_BT\left(\frac{T}{\theta_D}\right)^3\int_0^{\frac{\theta_D}{T}}\frac{z^3dz}{e^z-1} + \left(\frac{p-3}{p}\right)\frac{k_B\theta_E}{e^{\theta_D/T}-1}\right\}, \quad (12)$$

where δ is the electronic contribution to the average lattice displacement, θ_D is the Debye temperature, θ_E is the Einstein temperature, and p is the average number of phonon branches actually excited over the temperature range. G, F, c, and g are further material dependent constants. The Debye and Einstein temperature, extracted via a least-squares fit to the experimental data were θ_D = 413 K and θ_E = 87 K, with θ_D in very good agreement with the data gained via elastic moduli and electrical resistivity.

5. Summary/conclusion

Based on a detailed re-investigation, the constitution of the two phase diagrams Nb-Mn and Ta-Mn has been established from 600 °C to the melting range: the systems are characterized by $MgZn_2$-type Laves phases (C14), which are the only binary compounds in these systems but reveal extended homogeneity regions (each including the stoichiometric composition): $Nb_{1+x}Mn_{2-x}$ (62.5–73.0 at% Mn at 950 °C: $-0.19 \le x \le 0.125$) and $Ta_{1+x}Mn_{2-x}$ (59.5–68.5 at%

Mn: $-0.055 \le x \le 0.215$). About 20 samples have been prepared in each system, mainly by arc- or high frequency melting elemental ingots, in some cases also cold compacted powder blends. The investigation of the constitution comprised light optical and transmission and scanning electron microscopy (TEM and SEM) with energy dispersive (EDX) as well as wavelength dispersive (WDX) X-ray spectroscopy, X-ray powder (XPD) and single crystal (XSCD) diffraction, differential thermal analysis (DTA) and/or differential scanning calorimetry (DSC).

Whereas $NbMn_2$ melts congruently at $T_m(NbMn_2) = 1515 \pm 15$ °C, $TaMn_2$ melts incongruently with $T_m(TaMn_2) = 1797 \pm 40$ °C close to a depleted peritectic reaction. Both Laves phases engage in eutectic reactions with manganese: $\ell \leftrightarrow (Mn) + TMn_2$ ($T_{eut} = 1220 \pm 10$ °C at 4.9 at% Nb and $T_{eut} = 1234 \pm 10$ °C at 0.7 at% Ta, respectively). $NbMn_2$ also forms a eutectic with (Nb): $\ell \leftrightarrow (Nb) + NbMn_2$ at $T_{eut} = 1493 \pm 15$ °C at 53.2 at% Nb. In both systems, Mn reveals remarkably large maximum solid solubilities (at the reaction isotherms 1493 °C (Nb) and 1797 °C for (Ta)): 19.4 at% Mn in (Nb) and 21.3 at% Mn in (Ta).

Detailed investigation (SEM-WDX, TEM, Rietveld-XPD) on the stability and structure of the phases, "NbMn" and "TaMn", adopted earlier in the literature as binary system inherent compounds, clearly revealed these phases to be oxygen-stabilized adopting the Ti_4Ni_2O type (so-called eta(η)-phases) with modified Nb(Ta)/Mn site substitution to comply with the formula $Nb(Ta)_{3-x}Mn_{3+y}O_{1-y}$ (W_3Fe_3C-type). We also emphasize that no hints were found in our analyses for the existence of a μ-phase Nb_6Mn_7 or Ta_6Mn_7 (W_6Fe_7-type; space group $R\bar{3}m$). Magnetic susceptibility and magnetization measurements documented that both eta-phases η-$Nb_3Mn_3O_{1-y}$ and η-$Ta_3Mn_3O_{1-y}$ are ferromagnetic below $T_c \sim 77$ K, whereas the Laves phases $NbMn_2$, $TaMn_2$ are temperature independent paramagnetic. Furthermore, our DFT calculations define instability of the eta-phase Ta_3Mn_3 within the binary system (with respect to the weighted ratio of the C14 Laves phase $TaMn_2$ and pure bcc Ta). Additionally, the ab initio calculations confirmed (i) the stabilizing effect of oxygen on the eta-phase and (ii) the preference of oxygen atoms for sublattices in the sequence 16*d* (W_3Fe_3C-type)> 8*b*> 8*a* (W_6Fe_6C-type) in space group $Fd\bar{3}m$.

The experimentally derived constitution of the Nb-Mn and Ta-Mn systems served as the basis for CALPHAD calculations resulting in a complete set of optimized thermodynamic data for each system. The CALPHAD optimization was supported by DFT calculated heats of formation of various configurations of the C14 Laves phases.

Temperature dependent X-ray single crystal data (100–300 K) for $NbMn_2$ as well as room temperature SC data for $Ta_{1.05}Mn_{1.95}$ provided details on atom site distribution and thermal expansion (CTE-$NbMn_2$ $= 10.9 \times 10^{-6}$ K^{-1}). Thermodynamic and transport properties (specific heat, electrical resistivity and magnetic susceptibility/magnetization, from 2 to 300 K) classify both Laves phases with metallic behavior whilst mechanical properties (elastic moduli from DFT and nanoindentation as well as hardness and thermal expansion) group both Laves phases among rather hard (HV-$NbMn_2$ = 800, HV-$TaMn_2$ = 900) and brittle intermetallics ($K_{IC} = 1.1 \pm 0.5$ MPa $m^{1/2}$ for $NbMn_2$ and $K_{IC} = 1.5 \pm 0.2$ MPa $m^{1/2}$ for $TaMn_2$).

CRediT authorship contribution statement

All authors have contributed equally to the work.

Declaration of Competing Interest

The authors declare that they have no known competing financial interests or personal relationships that could have appeared to influence the work reported in this paper.

Acknowledgement

This research was supported by the Czech Science Foundation under projects GA 17-12844S and CZ.02.1.01/0.0/0.0/17_049/0008399. Thanks are also due to the OEAD for support via the bilateral WTZ CZ02 and to the MEYS CR via the bilateral Mobility 8J19AT011. Computational resources were supplied by the project "e-Infrastructure CZ" (e-INFRA CZ LM2018140) provided within the program "Large Infrastructures for Research, Experimental Development and Innovations" supported by the Ministry of Education, Youth and Sports of the Czech Republic.

Appendix A. Supporting information

Supplementary data associated with this article can be found in the online version at doi:10.1016/j.jallcom.2021.158715.

References

[1] C. Guerra, C. Aguilar, D. Guzman, M. Arancibia, P.A. Rojas, S. Lascano, L. Perez, Production and characterisation of mechanical properties of Ti-Nb-Ta-Mn alloys foams for biomedical applications, Powder Metall. 58 (1) (2015) 12–15.
[2] C. Guerra, M. Sancy, M. Walczak, D. Silva, C. Martinez, B. Tribollet, C. Aguilar, Evolution of oxide film on the internal porosity of Ti-30Nb-13Ta-2Mn alloy foam, Electrochim. Acta 283 (2018) 676–682.
[3] Y. Sun, W.W. Zhang, H.Q. Li, Preparation and properties of niobium-manganese composite electrode material, Diandu Yu Tushi 35 (1) (2016) 28–32.
[4] Y.S. Ko, H. Park, S.C. Jung, S.D. Wang, Development of high strength martensitic microalloyed steel for heavy-duty engine connecting rods, in: J.C. Zhao, M. Fahrmann, T. Pollock (Eds.), Proeedings of Symposium on Materials Design Approaches and Experiences, Indianapolis, IN, US, November 4–8 (2001) 151–16.
[5] P. Palzer, M. Otto, T. Evertz, Production of seamless medium manganese steel tubes, PCT International Application (2018), WO 2018083028 A1, May 11, 2018.
[6] M. Kawamori, J. Kinugasa, Y. Yonenaga, Y. Fukuta, M. Shimamoto, T. Sugimura, T. Sato, N. Nishizawa, M. Nagao, Effect of tantalum addition on pitting corrosion behavior of super duplex stainless steels - development of high corrosion resistant duplex stainless steels by inclusion control, Zair. Kankyo 64 (7) (2015) 320–323.
[7] H. Hatano, Effects of Nb and Mn on microstructure and toughness for simulated HAZ for 590 MPa class low carbon bainitic steels, Tetsu Hagane 91 (12) (2005) 875–881.
[8] E. Ekstroem, A. Le Febvrier, F. Bourgeois, B. Lundqvist, J. Palisaitis, P.O.Å. Persson, O. Caballero-Calero, M.S. Martin-Gonzalez, J. Klarbring, S.I. Simak, F. Eriksson, B. Paul, P. Eklund, The effects of microstructure, Nb content and secondary Ruddlesden-Popper phase on thermoelectric properties in perovskite $CaMn_{1-x}Nb_xO_3$ (x = 0 - 0.10) thin films, RSC Adv. 10 (13) (2020) 7918–7926.
[9] M. Nabi, T.M. Bhat, D.C. Gupta, Effect of pressure on electronic, magnetic, thermodynamic, and thermoelectric properties of tantalum-based double perovskites Ba_2MTaO_6 (M = Mn, Cr), Int. J. Energy Res. 43 (9) (2019) 4229–4242.
[10] B. Hamad, Ab initio investigations of the structural, electronic, and thermoelectric properties of Fe_2NbAl-based alloys, J. Mater. Sci. 51 (2016) 10887–10896.
[11] N. Parse, A. Attanusilp, W. Silpawilawan, K. Kurosaki, S. Pinitsoontorn, Enhancing thermoelectric properties of higher manganese silicide (HMS) by partial Ta substitution, J. Electron. Mater. 49 (5) (2020) 2726–2733.
[12] T. Massalski, Binary Alloy Phase Diagrams (second ed., ASM International, Materials Park, Ohio, USA. vol. 3, 1990, p. 2578; see also update by H. Okamoto, Supplemental literature review of binary phase diagrams: Ag-Sn, Al-Pd, Ba-Gd, Ba-Pr, Cu-P, Dy-Ni, Ga-Mn, Gd-Sb, Gd-Zr, Ho-Te, Lu-Sb, and Mn-Nb, J. Phase Equilib. Diffus. 35 (1) (2014) 105–116.
[13] V.N. Svechnikov, V.V. Pet'kov, Formation of Laves phases in alloys of manganese with transition metals of groups IV-Va (in Russian) Metallophysika, Akad. Nauk Ukr. SSR Inst. Metallofiz. 64 (1976) 24–28.
[14] A. Hellawell, The constitution manganese base alloys with metals of the second transition series, J. Less Common Met. 1 (1959) 343–347.
[15] B. Kuz'ma Yu, Phase equilibria in ternary hafnium-cobalt-boron, hafnium-nickel-boron, and niobium-manganese-boron systems, Visnik L'vivs'kogo Univ. Seriya Khimichna 14 (1972) 20–22 (in Ukrainian).
[16] S. Liu, B. Hallstedt, D. Music, Y. Du, Ab initio calculations and thermodynamic modeling for the Fe–Mn–Nb system, Calphad 38 (2012) 43–58.
[17] E.M. Savitskii, C.V. Kopetzkii, Phase diagram of the manganese-tantalum system, Russ. J. Inorg. Chem. 5 (11) (1960) 1274–1275 translated from Zh. Neorg. Khimii 64 (1960) 363-364.
[18] L. Kaufman, Coupled thermochemical and phase diagram data for tantalum based binary alloys, Calphad 15 (1991) 243–259.
[19] F.R. DeBoer, R. Boom, A.R. Miedema, Enthalpies of formation of liquid and solid binary alloys based on 3d metals II. Alloys of chromium and manganese, Physica B+C l13 (1982) 18–41.
[20] C. Colinet, A. Pasturel, P. Hicter, Trends in cohesive energy of transition metal alloys, Calphad 9 (1985) 71–99.

[21] A.T. Dinsdale, SGTE data for pure elements, Calphad 15 (1991) 317–425. Original data for Mn from A. Fernandez Guillermet, W. Huang, Int. J. Thermophys. 11 (1990) 949–969.
[22] C. Wang, C. Zhao, Z. Lin, X. Liu, Experimental determination and thermodynamic calculation of the phase equilibria in the Co-Mn-Ta system, Int. J. Mater. Res. 105 (12) (2014) 1179–1190.
[23] S.V. Meschel, P. Nash, X.Q. Chen, The standard enthalpies of formation of binary intermetallic compounds of some late 4d and 5d transition metals by high temperature direct synthesis calorimetry, J. Alloy. Compd. 492 (12) (2010) 105–115.
[24] X. Yan, X.Q. Chen, H. Michor, W. Wolf, V.T. Witusiewicz, E. Bauer, R. Podloucky, P. Rogl, Structural, thermodynamic, and electronic properties of Laves-phase $NbMn_2$ from first principles, x-ray diffraction, and calorimetric experiments, Phys. Rev. B 97 (2018) 1–10 125110.
[25] J. Rodriguez-Carvajal, Recent developments of the program FULLPROF, Physica B 55 (1993) 192 and T. Roisnel, J. Rodriguez-Carvajal, Mater. Sci. Forum 118 (2001) 378–381.
[26] Nonius Kappa CCD, Program Package COLLECT, DENZO, SCALEPACK, SORTAV, Nonius Delft, The Netherlands.
[27] G.M. Sheldrick, SHELX – Program for crystal structure refinement, Acta Crystallogr. A 64 (2008) 112–122; Windows version OSCAIL by P. McArdle, K. Gilligan, D. Cunningham, R. Dark, and M. Mahon, Natl. Univ. Ireland, Galway: Cryst. Eng. Comm. 6 (2004) 303–309. Windows version WINGX by L.J. Farrugia, J. Appl. Crystallogr. 32 (1999) 837–838.
[28] L.M. Gelato, E. Parthé, STRUCTURE TIDY-a computer program to standardize crystal structure data, J. Appl. Crystallogr. 20 (1987) 139–143; see also Program Typix, Gmelin Handbook of Inorganic and Organometallic Chemistry, vol. 1, Springer, N.Y., 1993, p. 186.
[29] INCA Energy-300 and INCA Wave 700, Oxford Instruments Analytical Ltd., UK, 2000.
[30] G. Binder, Studies of Spin-glass Materials with AC Susceptibility Measurements (in German) (Master thesis), TU-Wien, Austria, 2019.
[31] M. Rotter, H. Müller, E. Gratz, M. Doerr, M. Löewenhaupt, A miniature capacitance dilatometer for thermal expansion and magnetostriction, Rev. Sci. Instrum. 69 (7) (1998) 2742–2746.
[32] X.Q. Chen, Ab-initio Studies of Laves Phase Intermetallic Compounds (Ph.D. thesis), University of Vienna, Austria, 2003.
[33] P. Brož, F. Zelenka, J. Sopoušek, M. Hejduková, T. Kubčnová, O. Zobač, Thermal analysis and Knudsen effusion mass spectrometry combined in a specially-adapted commercial skimmer coupled instrument (Netzsch), Calphad 65 (2019) 86–92.
[34] G. Kresse, J. Furthmüller, Efficient iterative schemes for ab initio total-energy calculations using a plane-wave basis set, Phys. Rev. B 54 (1996) 11169–11172.
[35] G. Kresse, D. Joubert, From ultrasoft pseudopotentials to the projector augmented-wave method, Phys. Rev. B 59 (1999) 1758–1775.
[36] P.E. Blöchl, Projector augmented-wave method, Phys. Rev. B Condens. Matter 50 (20) (1994) 17953–17979.
[37] P.E. Blöchl, J. Kästner, C.L. Först, Chapter 1: Electronic structure method: augmented waves, pseudopotentials and the projector augmented wave method, in: Handbook of Materials Modeling, Springer, The Netherlands, 2005, pp. 93–119.
[38] J.P. Perdew, K. Burke, M. Ernzerhof, Generalized gradient approximation made simple, Phys. Rev. Lett. 77 (18) (1996) 3865–3868.
[39] J.P. Perdew, M. Ernzerhof, K. Burke, Rationale for mixing exact exchange with density functional approximations, J. Chem. Phys. 105 (22) (1996) 9982–9985.
[40] S. Kovaříková Oweis, M. Mazalová, J. Pavlů, P. Rogl, Ab initio study of Mn-based Laves and eta phases, to be published.
[41] X.Q. Chen, W. Wolf, R. Podloucky, P. Rogl, M. Marsman, Ab initio study of ground-state properties of the Laves-phase compound $ZrMn_2$, Phys. Rev. B 72 (2005) 1–11 054440.
[42] Pandat software, version 2014 2.0, CompuTherm LLC, Madison, Wisconsin, USA, 2014, ⟨http://www.computherm.com/⟩.
[43] H.L. Lukas, S.G. Fries, B. Sundman, Computational Thermodynamics, Cambridge University Press, Cambridge, 2007.
[44] H.S. Liu, J. Wang, Z.P. Jin, Thermodynamic optimization of the Ni–Sn binary system, Calphad 28 (2008) 363–370.
[45] J. Vřešťál, Recent progress in modelling of sigma-phase, Arch. Metall. 46 (3) (2001) 239–247.
[46] J. Havránková, J. Vřešťál, L.G. Wang, M. Šob, Ab initio analysis of energetics of σ-phase formation in Cr-based systems, Phys. Rev. B 63 (2001) 174104.
[47] P. Villars, K. Censual, Pearson's Crystal Data: Crystal Structure Database for Inorganic Compounds, ASM International, Materials Park, Ohio, USA, Release, 2019/20.
[48] D. Grüner, Investigations on the Nature of Laves Phases in Transition Metal Systems (in German) (Ph.D. thesis), TUDresden, Germany, 2007.
[49] W.B. Pearson, The Crystal Chemistry and Physics of Metals and Alloys, Wiley-Interscience, New York, USA, 1972. The 12-coordinated metallic radii in Tables 4–4 of this book have been taken from: E. Teatum, K. Gschneidner, and J. Waber, Report LA-2345, US Department of Commerce, Washington, D.C., USA, 1960.
[50] ICS database, 2019/20: Fachinformationszentrum Karlsruhe, Germany.
[51] P. Rogl, H. Nowotny, The mode of filling the voids in η-phases, Monatshefte Chem. 108 (1977) 1167–1180 (in German).
[52] P.A. Stadelmann, JEMS: Java Electron Microscopy Software, Switzerland, 2020; ⟨http://www.jems-swiss.ch⟩.
[53] P.A. Stadelmann, EMS - a software package for electron diffraction analysis and HREM image simulation in materials science, Ultramicroscopy 21 (1987) 131–145.
[54] N. Schönberg, Metallic ternary phases in the Mn-Ta-O system, Acta Metall. 3 (1955) 14–16.
[55] N. Schönberg, An X-ray investigation on ternary phases in the Ta-Me-N systems (Me = Ti, Cr, Mn, Fe, Co, Ni), Acta Chem. Scand. 8 (1954) 213–220.
[56] H. Holleck, F. Thümmler, Ternary complex-carbides, -nitrides, and -oxides with partially filled Ti_2Ni type structure, Monatshefte Chem. 98 (1967) 133–134 (in German).
[57] M. Drys, Phase equilibria in the niobium-gallium-manganese system at 900 °C, J. Less Common Met. 75 (1980) 261–265.
[58] Z. Blazina, R. Trojko, Structural investigations of the $Nb_{1-x}Si_xT_2$ and $Nb_{1-x}Al_xT_2$ (T = Cr, Mn, Fe, Co, Ni) systems, J. Less Common Met. 119 (1986) 297–305.
[59] P. Gupta, S.K. Singh, The manganese-niobium-nickel system, J. Phase Equilib. 16 (1995) 320–323.
[60] A.U. Khan, P. Brož, M. Premović, J. Pavlů, J. Vřešťál, X. Yan, D. Macciò, A. Saccone, G. Giester, P. Rogl, The Ti–Mn system revisited: experimental investigation and thermodynamic modelling, Phys. Chem. Chem. Phys. 18 (2016) 23326–23339.
[61] J. Pavlů, J. Vřešťál, M. Šob, Re-modeling of Laves phases in the Cr-Nb and Cr-Ta systems using first-principles results, Calphad 33 (2009) 179–186.
[62] S. Khmelevskyi, private communication, TU-Wien, Austria, 2020.
[63] A. Junod, D. Bichsel, J. Mueller, Modification of acoustic phonon spectra as a function of electron density of states in the superconductors of type A15, Helv. Phys. Acta 52 (1979) 580–596 (in French).
[64] A. Junod, T. Jarlborg, J. Mueller, Heat-capacity analysis of a large number of A15-type compounds, Phys. Rev. B 27 (1983) 1568–1585.
[65] S.F. Pugh, Relations between the elastic moduli and the plastic properties of polycrystalline pure metals, Philos. Mag. 45 (1954) 833–838.
[66] O.L. Anderson, A simplified method for calculating the Debye temperature from elastic constants, J. Phys. Chem. Solids 24 (1963) 909–917.
[67] G.D. Mukherjee, C. Bansal, A. Chatterjee, Thermal expansion study of ordered and disordered Fe_3Al: an effective approach for the determination of vibrational entropy, Phys. Rev. Lett. 76 (11) (1996) 1876–1879.